CMS Physics Analysis Summary

Contact: cms-pag-conveners-higgs@cern.ch 2013/03/07

Properties of the Higgs-like boson in the decay $\mathrm{H} \to \mathrm{ZZ} \to 4\ell$ in pp collisions at $\sqrt{s} = 7$ and 8 TeV

The CMS Collaboration

Abstract

The properties of the new boson with the mass around 125 GeV are reported. The boson is observed in the search for the standard model Higgs boson in the mass range $110 < m_H < 1000$ GeV in the $\mathrm{H} \to \mathrm{ZZ}$ decay channel. The search considers final states where both Z's decay to electron, muon, or tau lepton pairs. The analysis uses pp collision data recorded by the CMS detector at the LHC, corresponding to integrated luminosities of 5.1 fb^{-1} at $\sqrt{s} = 7$ TeV and 19.6 fb^{-1} at $\sqrt{s} = 8$ TeV. It makes use of the measured four-lepton mass, the mass uncertainty, kinematic discriminants, and information sensitive to the production mechanism, such as associated dijet characteristics and transverse momentum of the four-lepton system. The boson is observed in channels with electron and muon pairs with a local significance above the expected background of 6.7 standard deviations with the mass 125.8 ± 0.5 (stat.) ± 0.2 (syst.) GeV. The signal strength μ, relative to the expectation for the standard model Higgs boson, is measured to be $\mu = 0.91^{+0.30}_{-0.24}$. The signal strength modifiers associated with vector bosons and fermions in production are measured to be $\mu_V = 1.0^{+2.4}_{-2.3}$ and $\mu_F = 0.9^{+0.5}_{-0.4}$, thus consistent with the standard model expectations. The spin-parity of the boson is studied and the pure scalar hypothesis is found to be consistent with the observation when compared to six other spin-parity hypotheses. The data disfavour the pure pseudoscalar hypothesis 0^- with a $\mathrm{CL_s}$ value of 0.16%, and disfavour the pure spin-2 hypothesis of a narrow resonance with the minimal couplings to the vector bosons with a $\mathrm{CL_s}$ value of 1.5%. The spin-1 hypotheses are disfavoured with an even higher confidence. No other significant standard model Higgs-like excess is found in the search and upper limits at 95% confidence level exclude the range 130–827 GeV.

1 Introduction

The standard model (SM) of electroweak interactions [1–3] relies on the existence of the Higgs boson (H, with mass m_{H}), a scalar particle associated with the field responsible for the spontaneous electroweak symmetry breaking [4–9].

In July 2012, the CMS and ATLAS experiments announced [10, 11] the discovery of a new boson at a mass around 125 GeV, with properties compatible with the SM Higgs boson. A first measurement of its spin-parity state was reported by CMS [12], disfavoring the pure pseudoscalar hypothesis over the pure scalar one.

In this paper, an update of the properties of the new boson is presented in the channel $\mathrm{H} \to \mathrm{ZZ} \to 4\ell$ ($\ell = e, \mu$) using 5.1 fb^{-1} of pp data from the LHC collected in 2011 at $\sqrt{s}$ = 7 TeV, and 19.6 fb^{-1} collected in 2012 at $\sqrt{s}$ = 8 TeV, thus corresponding to the whole dataset. The properties examined are the mass, the signal strength relative to the expectation for the SM Higgs boson, the spin-parity quantum numbers, the corresponding fraction of a CP-violating contribution to the decay amplitude expressed through the fraction of the decay rate, and the fraction of the vector boson fusion (VBF) and associated top quarks or vector boson (VH) production mechanisms. In addition, a comprehensive search for other SM-like Higgs boson particles is performed through the $\mathrm{H} \to \mathrm{ZZ} \to 4\ell$ and $\mathrm{H} \to 2\ell 2\tau$ channels. The analysis is optimized for a SM-like Higgs boson particle in the mass range $110 < m_{\mathrm{H}} < 1000$ GeV. Searches for a SM Higgs boson have been previously performed at the LHC using about 5 fb^{-1} of 2011 data, in the $\mathrm{H} \to \mathrm{ZZ} \to 4\ell$ channel by ATLAS [13] and CMS [14], and in the $\mathrm{H} \to \mathrm{ZZ} \to 2\ell 2\tau$ channel by CMS [15]. The results from CMS excluded the SM Higgs boson in the mass range 127–600 GeV at 95% confidence level (CL) [16]. ATLAS excluded 111.4–116.6 GeV, 119.4–122.1 GeV, and 129.2– 541 GeV at 95% CL [17, 18]. Direct searches for the SM Higgs boson at the LEP $\mathrm{e^+e^-}$ collider have led to a lower-mass bound of $m_{\mathrm{H}} > 114.4$ GeV [19].

The analysis presented in this paper relies critically on the reconstruction, identification, and isolation of leptons. The high lepton reconstruction efficiencies are achieved for a ZZ system composed of two pairs of same-flavour and opposite-charge isolated leptons, $\mathrm{e^+e^-}$, $\mu^+\mu^-$, or $\tau^+\tau^-$, in the measurement range $m_{4\ell}, m_{2\ell 2\tau} > 100$ GeV. One or both of the Z bosons can be off-shell. The $\mathrm{Z} \to 4\ell$ resonance [20] is used in the mass range $70 < m_{4\ell} < 100$ GeV to cross-check our mass measurement method. The background sources include an irreducible four-lepton contribution from direct ZZ (or $\mathrm{Z}\gamma^*$) production via $\mathrm{q\overline{q}}$ annihilation and gg fusion. Reducible contributions arise from $\mathrm{Zb\overline{b}}$ and $\mathrm{t\overline{t}}$ where the final states contain two isolated leptons and two b jets producing secondary leptons. Additional background of instrumental nature arises from $\mathrm{Z} + \text{jets}$, $\mathrm{Z} + \gamma + \text{jets}$, and $\mathrm{WZ} + \text{jets}$ events where jets are misidentified as leptons.

Compared to the previous CMS analyses [12, 21], the main improvement arises from the introduction of a categorization based on the jet multiplicity in order to have optimal sensitivity to the different production mechanisms. The kinematic discriminant is also improved to fully take into account the interference coming from permutation of identical leptons, for both signal and background. The pure scalar hypothesis is compared to more alternative spin-parity hypothesis. The analysis also profits from additional trigger coverage for the 7 TeV data taking period and from refined methods to estimate the reducible background. In decay channels with τ leptons, the mass of the $\mathrm{Z} \to \tau\tau$ is now constrained to the nominal Z mass to take into account the undetected contribution of neutrinos. The electron, muon and photon reconstruction and selection methods remain unchanged, while for τ leptons the isolation requirements were retuned to better suppress the background from misidentified jets.

2 CMS detector and experimental methods

Particles produced in the pp collisions are detected in the pseudorapidity range $|\eta| < 5$, where $\eta = -\ln[\tan(\theta/2)]$ and θ is the polar angle with respect to the direction of the counterclockwise proton beam. The CMS detector comprises a superconducting solenoid, providing a uniform magnetic field of 3.8 T in the bore, equipped with silicon pixel and strip tracking systems ($|\eta| <$ 2.5) surrounded by a lead tungstate crystal electromagnetic calorimeter (ECAL) and a brass-scintillator hadronic calorimeter (HCAL) covering $|\eta| < 3.0$. A steel/quartz-fiber Cherenkov calorimeter extends the coverage to $|\eta| < 5$. The steel return yoke outside the solenoid is instrumented with gas ionization detectors used to identify muons up to $|\eta| < 2.4$. A detailed description of the detector is given in Ref. [22].

A complete reconstruction of the individual particles emerging from each collision event is obtained via a particle-flow (PF) technique. This uses the information from all CMS sub-detectors to identify and reconstruct individual particles in the collision event [23, 24]. They are classified into mutually exclusive categories: charged hadrons, neutral hadrons, photons, muons, and electrons.

For electrons, reconstructed candidates are first obtained in an inclusive way to gain efficiency. The electrons are reconstructed within the geometrical acceptance, $|\eta^{\mathrm{e}}| < 2.5$, and for transverse momentum $p_{\mathrm{T}}^{\mathrm{e}} > 7\,\mathrm{GeV}$. The reconstruction combines the information from clusters of energy deposits in the ECAL and the trajectory in the inner tracker [25–28]. The track-cluster matching is initiated either ″outside-in″ from energy cluster measurements, or ″inside-out″ from track reconstruction. Trajectories in the tracker volume are reconstructed using a dedicated modeling of the electron energy loss and fitted with a Gaussian sum filter. The contribution of the ECAL to the electron momentum and its uncertainty is determined via a multivariate regression approach. The regression is trained on a sample of simulated events, separately for barrel and endcaps. It uses the ratio of the true electron energy after final state radiation to the raw reconstructed energy as the target variable. The input variables involve in particular shower-shape variables. Electron identification relies on a multivariate technique that combines observables sensitive to the amount of bremsstrahlung along the electron trajectory, the geometrical and momentum matching between the electron trajectory and associated clusters, as well as shower-shape observables.

Muons are reconstructed within $|\eta^{\mu}| < 2.4$ and for $p_{\mathrm{T}}^{\mu} > 5\,\mathrm{GeV}$ [29]. The reconstruction combines the information from both the silicon tracker and the muon spectrometer. The matching between the inner and outer tracks is initiated either ″outside-in″, starting from a track in the muon system, or ″inside-out″, starting from a track in the silicon tracker. The PF muons are selected among the reconstructed muon track candidates by applying minimal requirements on the track components in the muon system and taking into account matching with small energy deposits in the calorimeters [30].

Corrections accounting for residual differences between data and simulation are applied to the muon momentum as well as on the ECAL energy before combining with the tracking momentum for electrons. Details about leptons momentum scale and resolution can be found in Appendix A.

Tau leptons are identified in their leptonic decay mode denoted τ_{ℓ}, with an electron or muon as measurable decay product, and in the semileptonic one denoted τ_{h}, with hadrons among the decay products. The PF particles are used to reconstruct τ_{h} with the “hadron-plus-strip” (HPS) algorithm [31]. The HPS algorithm optimizes the reconstruction and identification of specific τ_{h} decay modes. The π^0 components of the τ_{h} are first reconstructed and then combined with charged hadrons to reconstruct the τ_h decay modes. The neutrinos produced in all τ decays escape detection and are ignored in the reconstruction. The taus in this analysis are required to have $|\eta^{\tau_h}| < 2.3$ and $p_T^{\tau_h} > 20\,\text{GeV}$.

Jets are reconstructed using the anti-k_T clustering algorithm [32] with distance parameter $\Delta R = 0.5$, as implemented in the FASTJET package [33, 34]. Jet energy corrections are applied as a function of the jet E_T and η [35]. In addition, a multivariate discriminator is applied to separate jets from the primary interaction from those reconstructed due to energy deposits associated with pile-up. The discrimination is based on the differences in the jet shapes, in the relative multiplicity of charged and neutral components, and in the different fraction of transverse momentum which is carried by the hardest components. Within the tracker acceptance the jet tracks are also required to be compatible with the primary vertex. Jets are only considered if they have a transverse energy above 30 GeV and $|\eta| < 4.7$. In addition, they have to be separated from the lepton candidates and final-state radiation (FSR) photons (see below) by requiring $\Delta R = \sqrt{(\eta^{\ell/\gamma} - \eta^{jet})^2 + (\phi^{\ell/\gamma} - \phi^{jet})^2} > 0.5$.

The isolation of individual e or μ leptons is measured relative to their transverse momentum p_T^{ℓ}, by summing over charged and neutral particles in a cone $\Delta R = \sqrt{(\eta^{\ell} - \eta^{i})^2 + (\phi^{\ell} - \phi^{i})^2} < 0.4$ around the lepton direction at the interaction vertex:

$$R^{\ell}_{\text{Iso}} \equiv \left(\sum p_T^{\text{charged}} + \text{MAX}\left[0, \sum p_T^{\text{neutral}} + \sum p_T{}^{\gamma} - \rho \times A_{\text{eff}},\right]\right) / p_T^{\ell} \tag{1}$$

The $\sum p_T^{\text{charged}}$ is the scalar sum of the transverse momenta of charged hadrons originating from the primary vertex. The primary vertex is chosen as the vertex with the highest sum of p_T^2 of its constituent tracks. The $\sum p_T^{\text{neutral}}$ and $\sum p_T{}^{\gamma}$ are the scalar sums of the transverse momenta for neutral hadrons and photons, respectively. The latter excludes photons that are candidates for final-state radiation from the lepton (see below). Possible double counting in the isolation evaluation, caused by small differences between reconstructed electron candidates and those identified from the PF algorithm, is avoided by applying specific vetoes. The average transverse momentum flow density ρ is caculated in each event using a "jet area" technique [36]. It is defined as the median of the distribution for the neutral particles around all jets (any PF jet in the event having $p_T^{\text{jet}} > 3$ GeV). The effective area A_{eff} is the geometric area of the isolation cone times a correction factor which accounts for residual dependence of the isolation on pile-up as a function of η. The electrons or muons are considered isolated in the $\text{H} \to 4\ell$ analysis if $R^{\ell}_{\text{Iso}} < 0.4$. Tighter isolation requirements are imposed for e and μ leptons in the $\text{H} \to 2\ell 2\tau$ analysis depending on the assignment to either the $\text{Z} \to \ell^+\ell^-$, for which $R^{\ell}_{\text{Iso}} < 0.25$ is required, or to $\text{Z} \to \tau_{\ell} + \tau_h$, for which $R^{\ell}_{\text{Iso}} < 0.1$ is required for $\tau_e\tau_h$ and 0.15 for $\tau_\mu\tau_h$ final states respectively.

The isolation of τ lepton is calculated as the energy sum of the candidates in a solid cone of $\Delta R = 0.5$ around the reconstructed tau decay mode axis. The sum is adjusted for the average expected contribution from the pile-up in the form of a correction, calculated using charged hadron candidates not associated with the hard scatter vertex (E_T^{PU}) in a larger cone of $\Delta R = 0.8$ cone about the tau candidate. The isolation variable is defined as:

$$I^{\text{PF}} = \Sigma \left(p_T^{\text{charged}} + \text{MAX}(E_T^{\gamma} + E_T^{\text{neutral}} - 0.0729 \times E_T^{\text{PU}}, 0.0) \right) \tag{2}$$

where the correction factor of 0.0729, used in estimating the contribution to the isolation sum from neutral hadrons and photons, accounts for the difference in the cone sizes. Two standard working points are defined based on the value of the isolation sum corrected for the pile-up contribution: $I^{PF} < 1$ GeV for final states including one τ decaying hadronically and < 0.8 for final state with two of them. Standard criteria for the discrimination of τ from electron and muon leptons are also used.

The electron or muon pairs from Z decays should originate from the primary vertex. This is ensured by requiring that the significance of the impact parameter to the event vertex, $\mathrm{SIP_{3D}}$, satisfies $\mathrm{SIP_{3D}} = |\frac{\mathrm{IP}}{\sigma_{\mathrm{IP}}}| < 4$ for each lepton. The IP is the lepton impact parameter in three dimensions at the point of closest approach with respect to the primary interaction vertex, and σ_{IP} is its associated uncertainty.

The efficiencies for the product of reconstruction, identification, and isolation of primary e or μ leptons are measured in data, using a tag-and-probe technique [37] based on an inclusive sample of Z events. The measurements are performed in several bins of p_{T}^{ℓ} and $|\eta|$. The efficiencies for selecting electrons in the ECAL barrel (endcaps) varies from about 70% (60%) for $7 < p_{\mathrm{T}}^{\mathrm{e}} < 10\,\mathrm{GeV}$ to 85% (77%) at $p_{\mathrm{T}}^{\mathrm{e}} \simeq 10\,\mathrm{GeV}$, and reaches 95% (89%) for $p_{\mathrm{T}}^{\mathrm{e}} \geq 20\,\mathrm{GeV}$. It is about 85% in the transition region, $1.44 < |\eta| < 1.57$, between the ECAL barrel and endcaps, averaging over the whole p_{T} range. The muons are reconstructed and identified with efficiencies above $\sim$98% in the full $|\eta^{\mu}| < 2.4$ range. The efficiency of the τ_h reconstruction is approximately 50%. The performance for the tau lepton identification is discussed in Ref. [31].

Photons reconstructed within $|\eta^{\gamma}| < 2.4$ are possible FSR candidates. To be accepted as FSR, a reconstructed photon must either have a transverse momentum $p_{\mathrm{T}}^{\gamma} > 2\,\mathrm{GeV}$ and be found within $\Delta R < 0.07$ from a selected lepton candidate, or have $p_{\mathrm{T}}^{\gamma} > 4\,\mathrm{GeV}$ and be found isolated within $0.07 < \Delta R < 0.5$ around a selected lepton candidate. The photon isolation observable $R_{\mathrm{Iso}}^{\gamma}$ is the sum, divided by p_{T}^{γ}, of the transverse momenta of charged hadrons, other photons and neutral hadrons identified by the PF reconstruction in a cone of size $\Delta R = 0.3$ around the candidate photon direction. Isolated photons must satisfy $R_{\mathrm{Iso}}^{\gamma} < 1$.

The performance of the FSR selection algorithm has been measured using MC simulation samples, and the rate was verified with single-Z and data events. The photons within the acceptance for the FSR selection are measured with an efficiency of $\simeq$ 50% and with a mean purity of 80%. FSR photons are selected in 5% of single-Z events with muon pairs, and 0.5% of single-Z events with electron pairs. A gain of $\simeq$ 3% (2%, 1%) in efficiency is expected for the selection of $\mathrm{H} \to 4\mu$ ($2\mathrm{e}2\mu$, 4e) events in this analysis.

3 Datasets

Collision events are selected by the trigger system that requires the presence of a pair of electrons or a pair of muons, or a triplet of electrons. Triggers requiring an electron and a muon are also used. The minimal momenta of the first and second lepton are 17 and 8 GeV, respectively, for the double lepton triggers, while they are 15, 8 and 5 GeV for the triple electron trigger. The trigger efficiency within the acceptance of this analysis is greater than 98% for a Higgs boson signal with $m_{\mathrm{H}} > 120\,\mathrm{GeV}$ in the 4ℓ channels, and for $m_H > 200\,\mathrm{GeV}$ in the $2\ell 2\tau$ channels.

Monte Carlo (MC) samples for the SM Higgs boson signal and for background processes are used to optimize the event selection and to evaluate the acceptance and systematic uncertainties. The Higgs boson signals from gluon-fusion ($\mathrm{gg} \to \mathrm{H}$), and vector-boson fusion ($\mathrm{qq} \to \mathrm{qqH}$), are generated with POWHEG [38] at next-to-leading order (NLO). Signal samples with alternative spin-parity scenarios are generated with JHUGen [39] at Leading Order (LO). At low mass, the analysis is carried out in the framework of the narrow-width approximation, describing the Higgs lineshape with a Breit-Wigner distribution. This approximation breaks down at high mass (typically $m_H > 400\,\mathrm{GeV}$) due to the very large Higgs width ($\Gamma_\mathrm{H} > 70\,\mathrm{GeV}$). The lineshape is therefore corrected to match the results presented in [40–42] where the complex-pole scheme approach is described. Moreover, the interference between the Higgs boson signal produced by gluon-fusion and the background from $\mathrm{gg} \to \mathrm{ZZ}$ is taken into account, as suggested in Ref. [43]. The theoretical uncertainty on the shape of the resonance due to missing higher order (NLO) in the interference between background and signal is included, as well as the uncertainties due to electroweak corrections [41, 43, 44]. Additional samples of WH, ZH, and $\mathrm{t\bar{t}H}$ events are generated with PYTHIA [45]. Events at generator level are reweighted according to the total cross section $\sigma(\mathrm{pp} \to \mathrm{H})$, which contains contributions from gluon fusion up to next-to-next-to-leading order (NNLO) and next-to-next-to-leading log taken from Refs. [46–57] and from the weak-boson fusion contribution computed at NNLO in Refs. [49, 58–62]. The total cross section is scaled by the branching fraction $\mathcal{B}(\mathrm{H} \to 4\ell)$ calculated with PROPHECY4F, which includes NLO QCD and electroweak corrections and all interference effects at NLO [49, 63–66], in particular effects specific to the 4e and 4μ channels.

The SM background contribution from ZZ production via $\mathrm{q\bar{q}}$ is generated at NLO with POWHEG, while other diboson processes (WW, WZ) are generated with MADGRAPH [67] with cross sections rescaled to NLO predictions. The $\mathrm{gg} \to \mathrm{ZZ}$ contribution is generated with GG2ZZ [68]. The $\mathrm{Zb\bar{b}}$, $\mathrm{Zc\bar{c}}$, $\mathrm{Z}\gamma$, and $\mathrm{Z} +$ light jets samples are generated with MADGRAPH, as contributions to inclusive Z production, with cross sections rescaled to NNLO prediction for inclusive Z production. The $\mathrm{t\bar{t}}$ events are generated at NLO with POWHEG. The generation takes into account the internal initial-state and final-state radiation effects which can lead to the presence of additional hard photons in an event. For leading-order generators, the default set of parton distribution functions (PDF) used to produce these samples is CTEQ6L [69], while CT10 [70] is used for NLO generators.

All generated samples are interfaced with PYTHIA. All events are processed through a detailed simulation of the CMS detector based on GEANT4 [71] and are reconstructed with the same algorithms that are used for data. The simulations include pileup interactions matching the distribution of the number of such interactions observed in data.

4 Event selection and kinematics

The event selection is built to give a mutually exclusive set of signal candidates in the $\mathrm{H} \to 4\ell$ and $\mathrm{H} \to 2\ell 2\tau$ channels.

The signal candidates in the 4ℓ analysis are first selected. The selection uses well identified and isolated primary leptons. The lepton isolation requirements suppress the Z+jet, $\mathrm{Zb\bar{b}}$ and $\mathrm{t\bar{t}}$ backgrounds. The requirement on the significance of the impact parameter to the event vertex $\mathrm{SIP_{3D}} < 4$ further suppresses the $\mathrm{Zb\bar{b}}$ and $\mathrm{t\bar{t}}$ backgrounds. When building the Z candidates, only the FSR photons associated with the closest lepton and which make the "dressed" lepton-pair mass closer to the nominal Z mass are kept, with a maximum mass $m_{\ell\ell\gamma}$ of $100\,\mathrm{GeV}$. In the following, the presence of the photons in the 4ℓ kinematics is implicit. We require a Z candidate formed with a pair of leptons of the same flavour and opposite charge ($\ell^+\ell^-$). The pair with an invariant mass closest to the nominal Z mass is denoted m_{Z_1} and retained if it satisfies $40 < m_{\mathrm{Z}_1} < 120\,\mathrm{GeV}$. We then consider all remaining leptons and require a second pair of $\ell^+\ell^-$, with mass denoted m_{Z_2}, to satisfy $12 < m_{\mathrm{Z}_2} < 120\,\mathrm{GeV}$. The $12\,\mathrm{GeV}$ cut provides an optimal sensitivity for a Higgs boson mass hypothesis in the range $110 < m_\mathrm{H} < 160\,\mathrm{GeV}$. If more than one Z_2 candidate satisfies all criteria, the ambiguity is resolved by chosing the pair of leptons with the highest scalar sum of p_T. Among the four selected leptons forming the Z_1

and the Z_2, at least one should have $p_T > 20\,\text{GeV}$ and another one have $p_T > 10\,\text{GeV}$. These p_T thresholds ensure that the selected events have leptons on the high-efficiency plateau for the trigger. To further protect against leptons originating from hadron decays in jet fragmentation or from the decay of low-mass hadronic resonances, we require that any opposite-charge pair of leptons chosen among the four selected leptons (irrespective of flavour) satisfy $m_{\ell\ell'} > 4\,\text{GeV}$. The phase space for the search of the SM Higgs boson is defined by restricting the mass range to $m_{4\ell} > 100$ GeV.

To improve the sensitivity to the production mechanisms the event sample is split into two categories based on the jet multiplicity. The two categories are defined as follow:

- Category I: Events with fewer than two jets.
- Category II: Events with at least two jets.

In Category I the transverse momentum divided by the mass of the four lepton system ($p_T/m_{4\ell}$) is used to discriminate VBF and VH from gluon fusion. In Category II a linear discriminant (V_D) is formed combining two VBF sensitive variables, the difference in pseudorapidity ($\Delta\eta$) and the invariant mass of the two leading jets (m_{jj}). The discriminant is tuned to separate vector boson from gluon fusion processes. In Category I (II), about 5% (20%) of the signal events are expected to come from VBF production mechanism.

For the search in the $2\ell 2\tau$ final state, events are required to have one $Z_1 \to \ell^+\ell^-$ candidate with one lepton at $p_\text{T} > 20\,\text{GeV}$ and the other at $p_\text{T} > 10\,\text{GeV}$, and a $Z_2 \to \tau^+\tau^-$, with τ decaying into μ, e or τ_h. The leptons from the τ leptonic decays are required to have $p_\text{T}^{\ell} > 10\,\text{GeV}$. The τ_h are required to have $p_\text{T}^{\tau_\text{h}} > 20\,\text{GeV}$. The FSR recovery is not applied for the $2\ell 2\tau$ final state. The invariant mass of the reconstructed Z_1 is required to satisfy $60 < m_{\ell\ell} < 120\,\text{GeV}$, and that of the Z_2 to satisfy $m_\text{min} < m_{\tau\tau} < 90\,\text{GeV}$, where $m_\text{min} = 20\,\text{GeV}$ for $Z_2 \to \tau\tau \to e\mu$ final states, and 30 GeV for all others. At low $m_{\tau\tau}$, the Z_2 is restricted by the selection requirements on the p_T of the leptons. Thus, the $2\ell 2\tau$ final states contribute only to the "high-mass" part of the analysis ($m_{2\ell 2\tau} > 180$ GeV). To take into account the energy mismeasurement due to undetected neutrinos in τ decays, the Z_2 mass is constrained to the nominal Z mass by scaling the momenta of τ decay particles by a factor $91.2\,\text{GeV}/m_{Z_2}$. The scaling is applied after the full selection chain and affects the shape of the final $2\ell 2\tau$ mass and position of the mass peak.

Kinematics of the Higgs or exotic boson decay to ZZ final state has been extensively studied in the literature [39, 72–84]. Since the Higgs boson is spinless, the angular distribution of its decay products is independent of the production mechanism. Five angles $\vec{\Omega} = (\theta^*, \Phi_1, \theta_1, \theta_2, \Phi)$ defined in Fig. 1 and the invariant masses of the lepton pairs, m_{Z_1} and m_{Z_2}, fully describe the kinematics of the $H \to ZZ \to 4\ell$ process at a given mass of the four-lepton system in their centre-of-mass frame. These observables provide significant discriminating power between signal and background. Additional separation between signal and background from the transverse momentum of the four-lepton system is used by explicitly including this observable in the analysis, as discussed below.

We use a matrix element likelihood approach [10] to construct a kinematic discriminant (K_D) based on the probability ratio of the signal and background hypotheses, $K_D = \mathcal{P}_\text{sig}/(\mathcal{P}_\text{sig} + \mathcal{P}_\text{bkg})$, where the leading-order matrix elements define the probabilities for each value of $m_{4\ell}$. By construction, the discriminant is constrained to be between zero and one, and the relative normalization of probabilities is chosen to equate probabilities for signal and background distributions above and below 0.5, respectively. Several choices of matrix elements have been studied for signal and $q\bar{q}/gg \to ZZ/Z\gamma^*$ background, including analytical parameterization [39, 83, 84], JHUGEN [39, 83], MCFM [85–87] implemented within the MELA framework [10] and

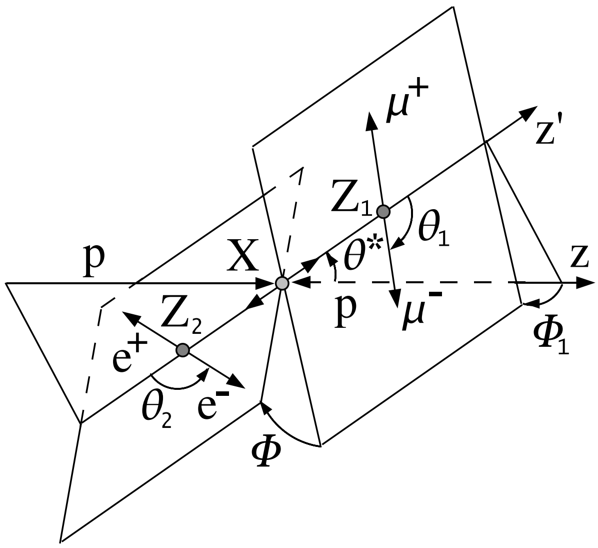

Figure 1: Illustration of the production and decay of a particle X $ab \to X \to Z_1Z_2 \to 4\ell$ with the two production angles θ^* and Φ_1 shown in the X rest frame and three decay angles θ_1, θ_2, and Φ shown in the Z_i and X rest frames, respectively [39].

MADGRAPH [67] implemented within the MEKD framework [88]. Different matrix elements were found to provide nearly identical performance for the processes implemented in common. The machine trained techniques such as boosted decision trees or Bayesian neural networks were also investigated. They give similar results as the matrix element approaches. The kinematic discriminants for the baseline analysis is built out of matrix element for the signal hypotheses taken from JHUGEN and matrix elements for the qq $\to$ ZZ background taken from MCFM.

5 Background control and systematics

We rely on MC simulation to evaluate the local density ($\Delta N/\Delta m_{4\ell}$) of events expected as a function of the mass $m_{4\ell}$ from the ZZ background. Following the prescription used in the previous analysis, the cross section for ZZ production at NLO is calculated with MCFM [85–87]. This includes the dominant process of $q\overline{q}$ annihilation, as well as gluon induced production. The theoretical uncertainties are computed as a function of $m_{4\ell}$, varying both the QCD renormalisation and factorization scales and the PDF set, following the PDF4LHC recommendations [89–93]. The uncertainties for the QCD and PDF scales for each final state are on average 8%. The number of predicted ZZ $\to 4\ell$ events and their uncertainties after the signal selection are given in Table 1.

To estimate the reducible ($Zb\overline{b}$, $t\overline{t}$) and instrumental (Z + light jets, WZ + jets) backgrounds, a Z_1+X background control region, well separated from the signal region, is defined. In addition, a sample $Z_1 + \ell_{\mathrm{reco}}$, with at least one reconstructed lepton object, is defined for the measurement of the lepton misidentification probability — the probability for a reconstructed object to pass the isolation and identification requirements. The contamination from WZ in these events is suppressed by requiring the imbalance of the measured energy deposition in the transverse plane to be below 25 GeV. The lepton misidentification probability is compared, and found compatible, with the one derived from MC simulation.

The event rates measured in the background control region are extrapolated to the signal region. Two different approaches are used. They differ in the way the contribution from electrons coming from photon conversions is handled. Both start by relaxing the isolation and identification criteria for two additional reconstructed lepton objects. A first approach follows from the previous CMS analysis [14]. It aims at estimating all contributions of reducible background in one single step. The additional pair of leptons is required to have the same charge (to avoid signal contamination) and same flavour ($e^{\pm}e^{\pm}$, $\mu^{\pm}\mu^{\pm}$), a reconstructed invariant mass $m_{Z_2} > 12\,\mathrm{GeV}$, and $m_{4\ell} > 100\,\mathrm{GeV}$. The expected number of Z+X background events in the signal region is obtained by taking into account the lepton misidentification probability for each of the two additional leptons. In this method, this probability is corrected for the difference in the fraction of electrons from photon conversions between the control region and the $Z_1 + \ell_{\mathrm{reco}}$ sample. The second method, used also for $\tau\tau$ final states, employs the control region with two opposite-sign leptons failing the isolation and identification criteria. In addition, a control region with three passing and one failing lepton is also used to account for contributions from backgrounds with three prompt leptons and one misidentified lepton. The validity of the two methods is assessed with closure tests in the simulation and checks with data on samples using relaxed charge and flavour requirements. Comparable background counts in the signal region are found within uncertainties from both methods. An envelope comprising these results is used as the final estimate in Table 1.

Systematic uncertainties are evaluated from data for trigger (1.5%), and combined lepton reconstruction, identification and isolation efficiencies (varying from 2.9% to 4.3% in the 4μ channel and from 5.5% to 11% in $4e$ channel, depending on the considered mass). The uncertainty associated with τ_{h} identification and isolation is 6%. Uncertainties on τ_{h} energy scale (3%) contribute to variations in the shape of the mass spectrum. Samples of $Z \to \ell\ell$, $\Upsilon \to \ell\ell$ and $J/\psi \to \ell\ell$ are used to set and validate the absolute momentum scale and resolution. The systematic uncertainty on the muon momentum scale is estimated to be 0.1% which translates into a 0.1% uncertainty on the 4μ mass. For electrons, a p_{T} dependency is observed, but it affects only marginally the four-lepton mass with a propagated uncertainty of 0.3% for the 4e channel. The effect of the energy resolution uncertainties is taken into account by introducing a 20% uncertainty on the simulated width of the signal mass peak. More details are given in Appendix A. Additional systematic uncertainties arise from the limited statistical precision in the reducible background control regions as well as the difference in background composition between the control regions and the sample on which the lepton misidentification probability is derived. The total uncertainty on the reducible background estimate for the $2\ell 2\tau$ final state is approximately 30%. All reducible and instrumental background sources are derived from control regions, and the comparison of data with the background expectation in the signal region is independent of the uncertainty on the LHC integrated luminosity of the data sample. This uncertainty (2.2% at 7 TeV, 4.4% at 8 TeV) [94] enters the evaluation of the ZZ background and in the calculation of the cross section limit through the normalisation of the signal. Systematic uncertainties on the Higgs boson cross section (17 – 20%) and branching fraction (2%) are taken from Ref. [49]. In Category II, additional systematics on ZZ background normalization comes from the comparison of POWHEG and MADGRAPH. In Category II, a 30% normalization uncertainty is taken into account for the $gg \to H + 2$ jets signal cross-section, while 10% is retained for the VBF production. Additional shape uncertainties for Category I and II are described in the next section.

6 Results

The reconstructed four-lepton invariant-mass distribution for the 4ℓ, combining the 4e, 4μ, and $2e2\mu$ channels, is shown in Fig. 2 and compared with the expectation from SM background processes. The observed distribution is in good agreement with the expectation. The $Z \to 4\ell$ resonance peak at $m_{4\ell} = m_Z$ is observed with normalization and shape as expected. The measured distribution at higher mass is dominated by the irreducible ZZ background. A clear peak around $m_{4\ell} = 126$ GeV is seen, confirming the results reported in [10].

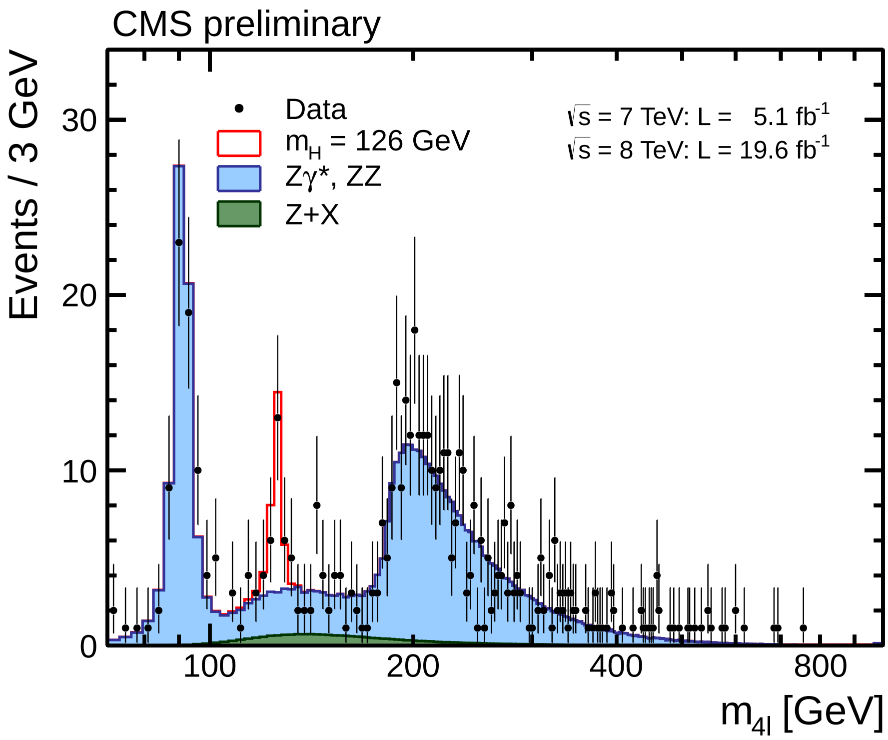

Figure 2: Distribution of the four-lepton reconstructed mass in the full mass range for the sum of the 4e, 4μ, and $2e2\mu$ channels. Points represent the data, shaded histograms represent the background and the unshaded histogram the signal expectation. The expected distributions are presented as stacked histograms. The measurements are presented for the sum of the data collected at $\sqrt{s} = 7$ TeV and $\sqrt{s} = 8$ TeV. No event is observed for $m_{4\ell} > 800$ GeV.

The reconstructed visible mass distribution after Z_2 scaling for the $2\ell 2\tau$ selection, combining all the $\ell^+\ell^-\tau^+\tau^-$ final states, is shown in Fig. 3. The measured distribution is well described by the SM background expectation.

The number of candidates observed as well as the estimated background are reported in Table 1, for the selection in the full mass measurement range for the SM-like Higgs boson search, $100 < m_{4\ell}, m_{2\ell 2\tau} < 1000$ GeV. The expected number of signal events is also given for several SM-like Higgs boson mass hypotheses. The observed event rates for the various channels are compatible with SM background expectation.

The distributions of the kinematic discriminant K_D versus the four-lepton reconstructed mass $m_{4\ell}$ are shown for the selected events and compared to SM background expectation in Fig. 4. The distribution of events in the $(m_{4\ell}, K_D)$ plane is seen to agree well with the SM expectation

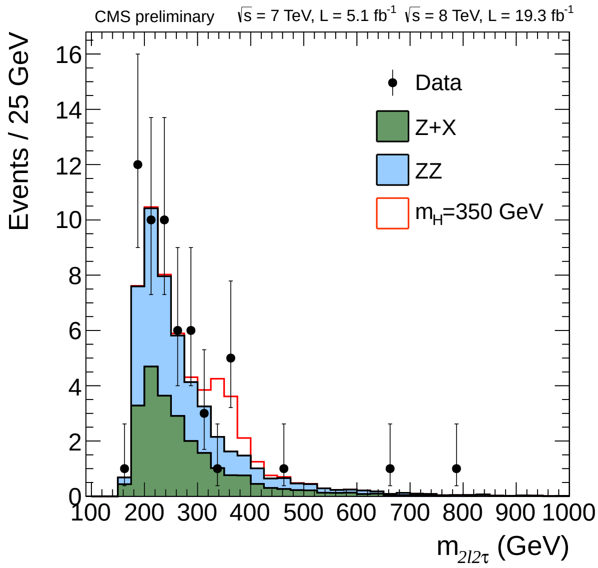

Figure 3: Distribution of the four-lepton reconstructed mass in full mass range for the sum over all $\ell^+\ell^-\tau^+\tau^-$ channels (right). Points represent the data, shaded histograms represent the background and the unshaded histogram the signal expectation. The expected distributions are presented as stacked histograms. The measurements are presented for the sum of the data collected at $\sqrt{s} = 7\,\text{TeV}$ and $\sqrt{s} = 8\,\text{TeV}$. No event is observed for $m_{2\ell 2\tau} > 800\,\text{GeV}$.

in the high mass range (Fig. 4, right).

The selected events are split into twelve sub-categories based on three final states, two running periods (7 and 8 TeV) and two jet categories. These events are examined for 187 hypothetical SM-like Higgs boson masses in a range between 110 GeV and 1000 GeV, where the mass steps are optimized to account for the expected width and resolution for the measurement of m_{H} [95]. For the events in Category I, a three dimensional model of $(m_{4\ell}, K_D, p_T/m_{4\ell})$ is utilized for masses below 180 GeV while for higher masses a two dimensional model of $(m_{4\ell}, K_D)$ is used. In Category II a three dimensional model of $(m_{4\ell}, K_D, V_D)$ is used for the full mass range. We adopt the modified frequentist construction $\mathrm{CL_s}$ [95–97] as the primary method for

Table 1: The number of event candidates observed, compared to the mean expected background and signal rates for each final state. For the Z +X background, the estimates are based on data. The results are given integrated over the full mass measurement range for the SM-like Higgs boson search from 100 to 1000 GeV and for 2011 and 2012 data combined.

Channel	4e	4μ	$2e2\mu$	$2\ell 2\tau$
ZZ background	78.9 ±10.9	118.9 ±15.5	192.8 ±24.8	27.4 ±3.6
Z+ X	6.5 ± 2.6	3.8 ± 1.5	9.9 ± 4.0	22.9 ±7.8
All background expected	85.5 ± 11.2	122.6 ± 15.5	202.7 ± 25.2	50.3 ±8.6
m_H = 125 GeV	3.5 ±0.5	6.8 ±0.8	8.9 ±1.0	–
m_H = 126 GeV	3.9 ±0.6	7.4 ±0.9	9.8 ±1.1	–
m_H = 500 GeV	5.1 ±0.6	6.8 ±0.8	12.0 ±1.3	3.7 ±0.4
m_H = 800 GeV	0.7 ±0.1	0.9 ±0.1	1.6 ±0.2	0.4 ±0.1
Observed	86	125	240	57

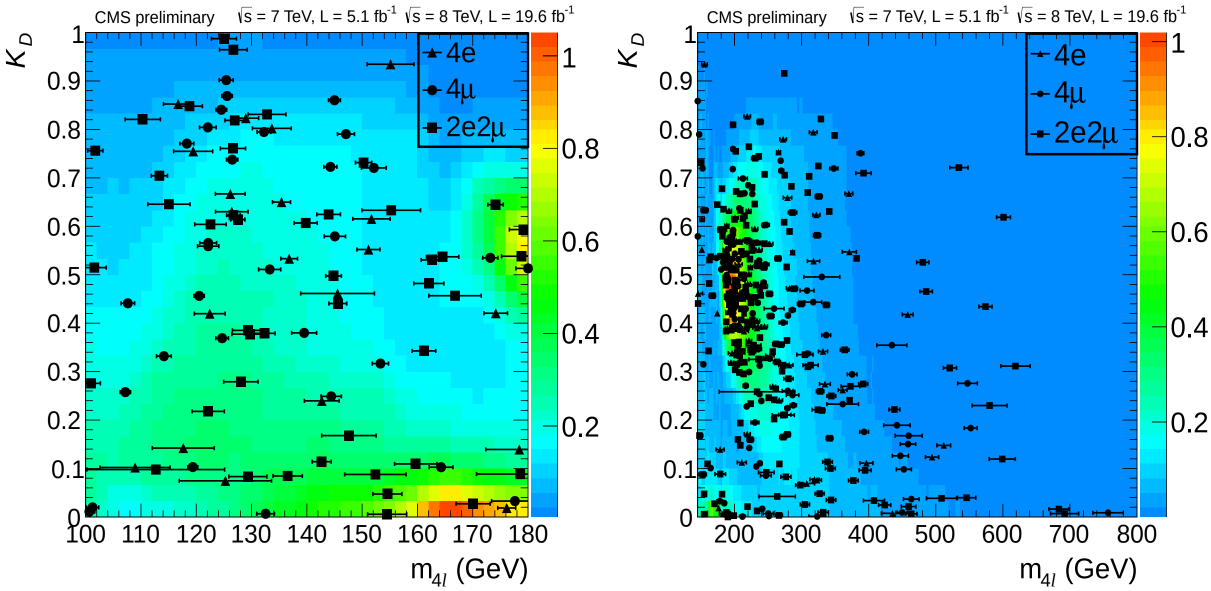

Figure 4: Distribution of the kinematic discriminant K_D versus the four-lepton reconstructed mass $m_{4\ell}$ in the low-mass (left) and high-mass (right) regions. The contours represent the expected relative density of signal events. The points show the data and the measured invariant mass uncertainties as horizontal bars. No event is observed for $m_{4\ell} > 800$ GeV.

reporting limits. As a complementary method to the frequentist paradigm, we use the Bayesian approach [98] and find consistent results.

The probability distribution of $\mathcal{P}(m_{4\ell})$ for the background is parametrised with empirical functions using MC simulation for ZZ background and data control regions for $Z+X$ background. The reconstructed signal $m_{4\ell}$ distributions are described with a relativistic Breit-Wigner parametrization convoluted with a double-sided Crystal Ball function [99]. The correlated three-dimensional $(m_{4\ell}, K_D, X)$ distribution is described by the one-dimensional probability distribution $\mathcal{P}(m_{4\ell})$ multiplied by a two-dimensional template distribution of $(m_{4\ell}, K_D)$ normalized in the K_D dimension and a two-dimensional $(m_{4\ell}$, X) template distribution normalized in the X dimension, where X=V_D for Category I and X=$p_T/m_{4\ell}$ for Category II.

The kinematic discriminant template distribution is obtained from simulation for both signal and ZZ background, accounting for interference effects of identical leptons in the final state. It has been verified that the K_D distribution of the $Z+X$ background is consistent with that of the ZZ background, and any potential small difference is accounted for in the systematic uncertainties.

The gluon fusion signal template distribution for $p_T/m_{4\ell}$ is obtained from simulation after reweighting the p_{T} spectrum by the next-to-next-to-leading-logarithm (NNLL)+NLO expectations including effects from resummation [100–102] while the vector boson fusion and ZZ background spectra from POWHEG are used. For the associated production process the leading order spectrum by PYTHIA is used and the difference due to NLO effects is considered as a systematic uncertainty. The template distributions for the VBF discriminant V_D are taken from POWHEG simulation for signal and SM ZZ processes.

Template distributions are derived from simulation or control regions for both $p_T/m_{4\ell}$ and V_D.

Alternative shapes are introduced to account for statistical and systematic errors on these observables. In the Category I, alternative shapes of V_D arise from the comparison with different generators and underlying event tunes. The change in V_D shape is found to be negligible for variations of the jet energy scale. Several uncertainties are taken into account for the shape of $p_T/m_{4\ell}$: QCD and PDF scales variation, resummation effects, as well as the effect of finite top quark mass in gluon fusion production mechanism.

For the $2\ell 2\tau$ channels, signal and background shape templates are taken from simulation, with the background yields normalized to the data-driven yields described above. Shape variations due to τ energy scale uncertainties are accounted for by vertical template morphing. Due to the limited number of simulated events, the reducible background shape was taken with relaxed isolation requirements on the second Z boson. Normalizations for backgrounds vary within the uncertainties. All systematic uncertainties are included in the likelihood with log-normal distributions.

The upper limits obtained from the combination of the 4ℓ and $2\ell 2\tau$ channels are shown in Fig. 5 (left). The SM-like Higgs boson is excluded by the four-lepton channels at 95% CL in the range 130–827 GeV (for an expectation of 113.5–778 GeV). The local p-values, representing the

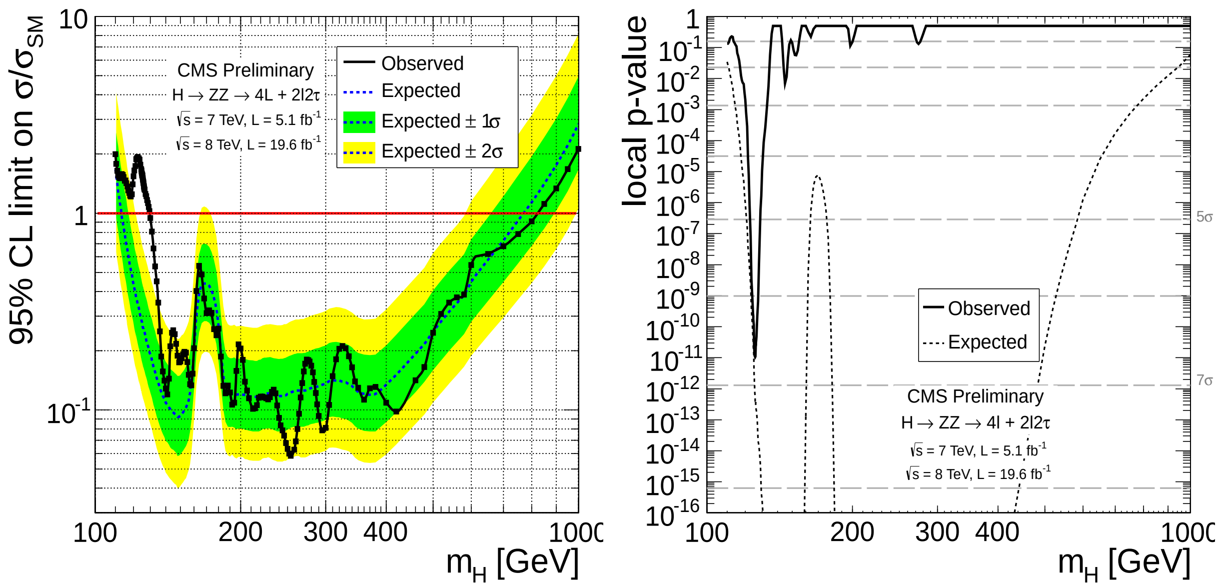

Figure 5: Observed and expected 95% CL upper limit (left) on the ratio of the production cross section to the SM expectation. The expected 68% and 95% CL ranges of expectation for the background-only model are also shown with green and yellow bands, respectively. Significance of the local excess (right) with respect to the SM background expectation as a function of the Higgs boson mass in the full interpretation mass range 110-1000 GeV.

significance of local excesses relative to the background expectation, are shown for the full mass range as a function of m_H in Fig. 5 (right). The minimum of the local p-value is reached around $m_{4\ell} = 125.8$ GeV, near the mass of the new boson [10], and corresponds to a local significance of 6.7σ (for an expectation of $7.2\ \sigma$). This constitutes an observation of the new boson in the four-leptons channel alone. As a cross-check, we have also studied 1D ($m_{4\ell}$) and 2D ($m_{4\ell}$, K_D) models (see Fig. 6, right) and observed a local significance of 4.7 and 6.6 σ, for an expectation of 5.6 and 6.9 σ, respectively.

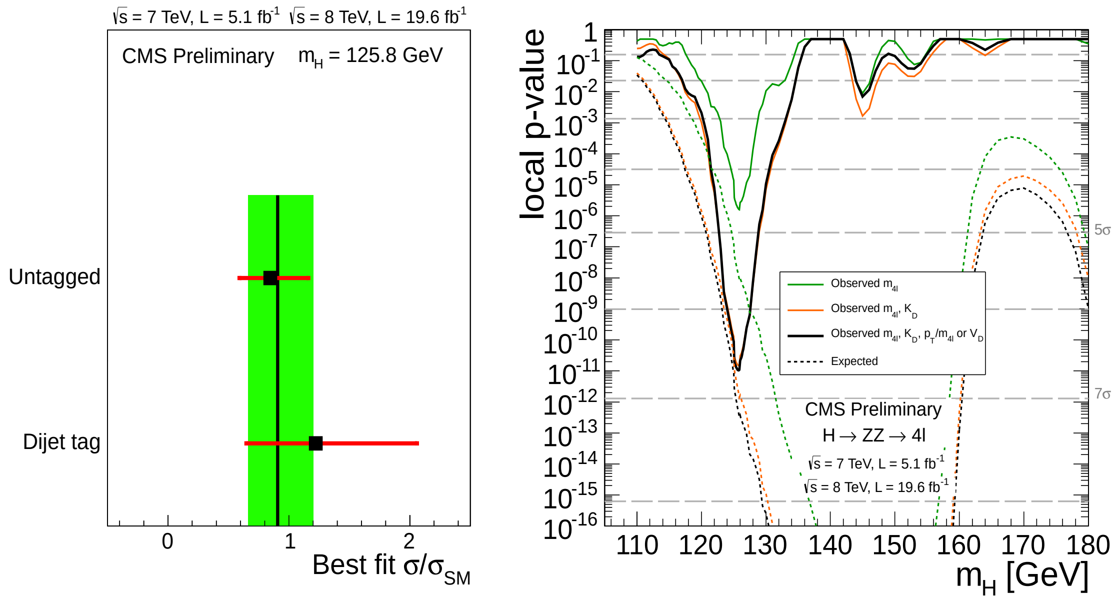

Figure 6: Values of $\mu = \sigma/\sigma_{SM}$ for the two categories (left). The vertical line shows the combined μ, together with its associated $\pm 1\sigma$ uncertainties shown as green band. The horizonthal bars indicate the $\pm 1\sigma$ uncertainties on μ for the different categories. The uncertainties include both statistical and systematic contributions. Significance of the local excess (right) with respect to the SM background expectation as a function of the Higgs boson mass for the 1D ($m_{4\ell}$), 2D ($m_{4\ell}$, K_D) and 3D ($m_{4\ell}$, K_D, $p_T/m_{4\ell}$ or V_D) models. The results are shown for the full data sample in the low mass region only.

Table 2 reports the number of observed and predicted events in the mass region near the signal, from 110 to 160 GeV, where the background is expected to be relatively flat.

Table 2: The number of event candidates observed, compared to the mean expected background and signal rates for each final state. For the Z +X background, the estimates are based on data. The results are given integrated in the mass range from 110 to 160 GeV.

Channel	4e	4μ	$2e2\mu$	4ℓ
ZZ background	6.6 $\pm$0.8	13.8 $\pm$1.0	18.1 $\pm$1.3	38.5 $\pm$1.8
Z+ X	2.5 $\pm$ 1.0	1.6 $\pm$ 0.6	4.0 $\pm$ 1.6	8.1 $\pm$2.0
All background expected	9.1 $\pm$ 1.3	15.4 $\pm$ 1.2	22.0 $\pm$ 2.0	46.5 $\pm$2.7
m_H = 125 GeV	3.5 $\pm$0.5	6.8 $\pm$0.8	8.9 $\pm$1.0	19.2 $\pm$1.4
m_H = 126 GeV	3.9 $\pm$0.6	7.4 $\pm$0.9	9.8 $\pm$1.1	21.1 $\pm$1.5
Observed	16	23	32	71

The distribution of the four-lepton reconstructed mass for the sum of the 4e, 4μ, and $2e2\mu$ channels, and the distribution of the kinematic discriminant K_D versus the four-lepton reconstructed mass $m_{4\ell}$ are shown in Fig. 7 in the low mass range. A signal-like clustering of events is apparent at high values of K_D, as seen in Fig. 7 (right), and for $m_H \approx 126$ GeV. The K_D distribution is shown in a restricted $m_{4\ell}$ interval in Fig. 8 (left) and as an illustration, the reconstructed four-lepton invariant-mass distribution is shown in Fig. 8 (right) for events with $K_D > 0.5$. Figure 9 shows the reconstructed invariant masses of the Z_1 and Z_2 in a restricted mass range.

The distributions of the VBF discriminant V_D and $p_T/m_{4\ell}$ are presented in Fig. 10. The trans-

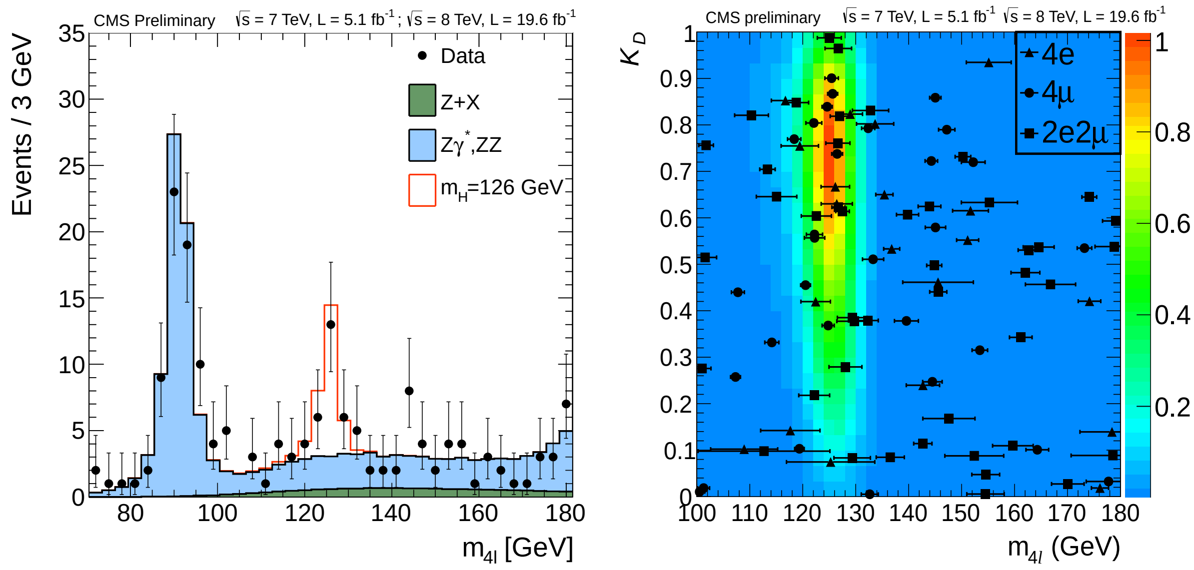

Figure 7: Distribution of the four-lepton reconstructed mass for the sum of the 4e, 4μ, and $2e2\mu$ channels (left). Points represent the data, shaded histograms represent the background and the unshaded histogram the signal expectation. Distribution of the kinematic discriminant K_D versus the four-lepton reconstructed mass $m_{4\ell}$ (right) with contours shown for the expected relative density of signal events for $m_H = 126$ GeV. The points show the data with measured invariant mass uncertainties as horizontal bars.

verse momentum spectrum shows good agreement for a SM Higgs hypothesis in Category I. In Category II no events with high rank of the V_D ($V_D > 0.5$), denoting VBF production, are observed.

The signal strength μ, relative to the expectation for the SM Higgs boson, is measured to be $\mu = 0.91^{+0.30}_{-0.24}$ at 125.8 GeV. It is found to be $0.85^{+0.32}_{-0.26}$ in Category I and $1.22^{+0.84}_{-0.57}$ in Category II, as reported in Fig. 6 (left). Using simulation it is found that the kinematic discriminant K_D distribution for the signal at a mass around $m_H = 126$ GeV is similar for a scalar, pseudo-scalar, vector, pseudo-vector or a spin-two resonance with the minimal couplings [39]. Therefore the analysis presented is nearly model-independent in the low-mass region. In the following, we discuss in more detail the measurements of the new boson's properties.

6.1 Mass measurement

The mass measurement of the new resonance is performed with a three-dimensional fit using for each event the four-lepton invariant mass, the associated per-event mass error, and the kinematic discriminant. Per-event errors on the 4-lepton invariant mass are calculated from the individual lepton momentum errors. Individual lepton momentum errors are computed for muons using the full error matrix, as obtained from the muon track fit, and for electrons using the estimated momentum error, as obtained from the combination of the ECAL and tracker measurements. More details are given in Appendix A. The shape of the per-event error distributions for the signal and the ZZ background are extracted from the MC simulation and are cross-checked with data in the control region for the ZZ background. The corresponding shape for the reducible background is extracted from the control regions in data. The correlation between per-event errors and the kinematical discriminant can be neglected, as verified with MC

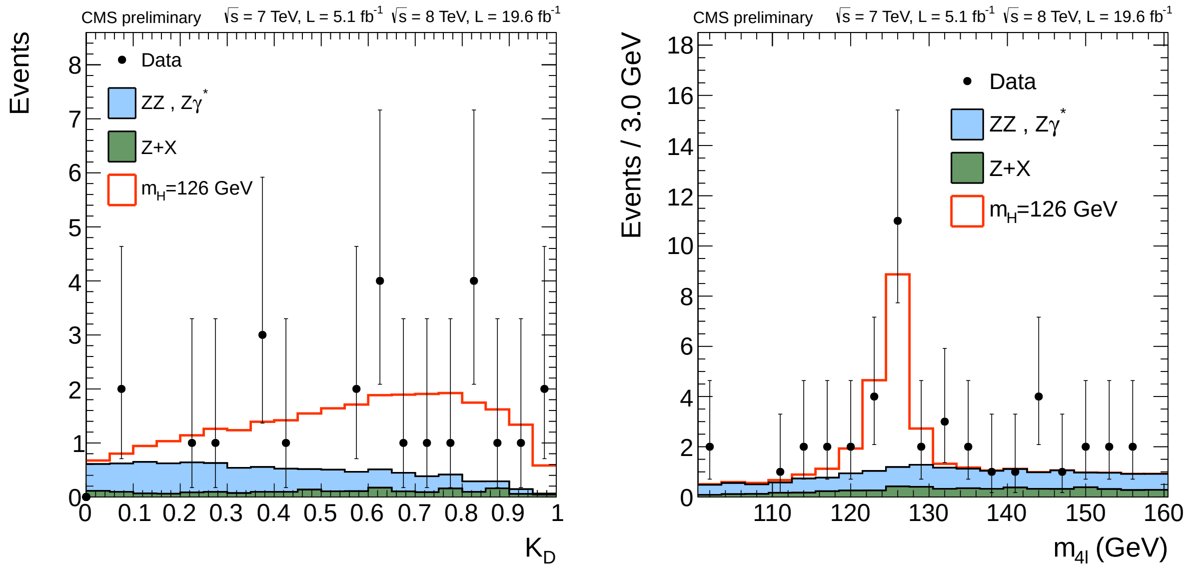

Figure 8: Distribution of the kinematic discriminant for events in the mass region $121.5 < m_{4\ell} < 130.5\,\text{GeV}$ (left). Distribution of the four-lepton reconstructed mass for the sum of the 4e, 4μ, and $2e2\mu$ channels for events with a value $K_D > 0.5$ of the kinematic discriminant (right). Points represent the data, shaded histograms represent the background and unshaded histograms the signal expectation. The measurements are presented for the sum of the data collected at $\sqrt{s} = 7\,\text{TeV}$ and $\sqrt{s} = 8\,\text{TeV}$.

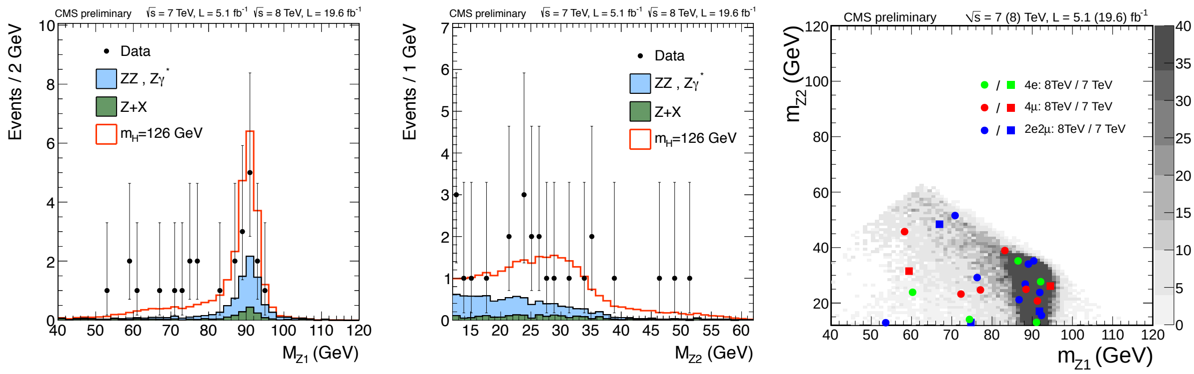

Figure 9: Distribution of the Z_1 (left) and Z_2 (center) reconstructed invariant masses and correlation between the two (right) in the mass region $121.5 < m_{4\ell} < 130.5\,\text{GeV}$ for the sum of the 4ℓ channels. Points represent the data, shaded histograms represent the background. Signal expectation at $m_{\rm H} = 126\,\text{GeV}$ is shown as the unshaded histogram (left and center) or as grey contour (right).

simulation. Figure 11 (left) shows the one-dimensional likelihood scan versus Standard Model Higgs boson mass performed under the assumption that its width is much smaller than the detector resolution. The resulting fit gives $m_{\rm H} = 125.8 \pm 0.5$ (stat.) ± 0.2 (syst.) GeV. The systematic uncertainty accounts for the effect on the mass scale of the lepton momentum scale and resolution as described in 5.

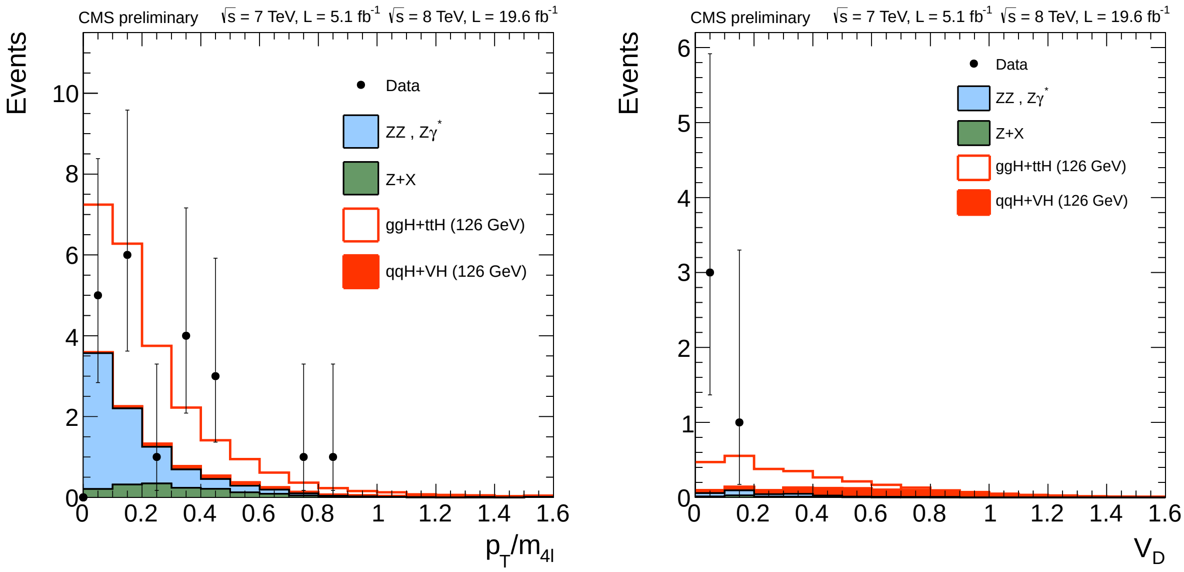

Figure 10: Distribution of $p_{\mathrm{T}}/m_{4\ell}$ in Category I (left). Distribution of the VBF discriminant in Category II (right). Only events in the mass region $121.5 < m_{4\ell} < 130.5\,\mathrm{GeV}$ are considered.

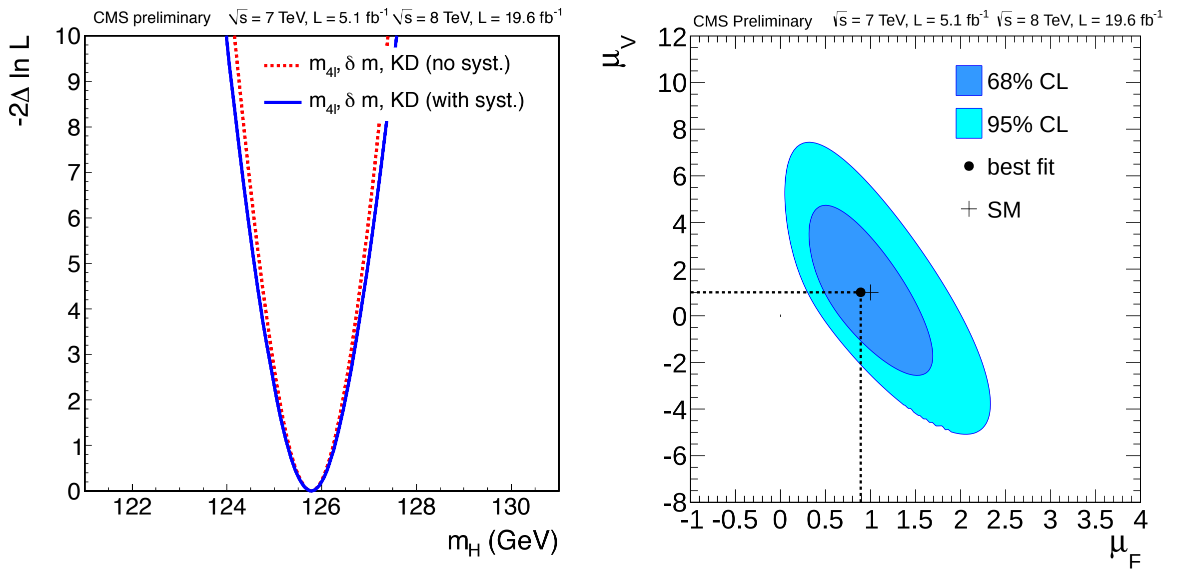

Figure 11: 1D test statistics $q(m_{\mathrm{H}}) = -2\Delta \ln \mathrm{L}$ scan vs tested Higgs boson mass m_{H}, obtained from the 3D test statistics profiling the minimum of the signal strengths, with and without systematics (left). Likelihood contours on the signal strength modifiers associated with fermions (μ_F) and vector bosons (μ_V) shown at 68% and 95% CL (right).

6.2 Measurement of production mechanisms

The jet categorization and the utilization of the transverse momentum spectrum and vector boson fusion sensitive variables are used to disentangle the production mechanisms of the observed new state. The production mechanisms are split into two categories depending on whether the production is induced by vector bosons (VBF, ZH, WH) or fermions (gluon fusion loop with quarks, ttH). Two respective signal strength modifiers (μ_F, μ_V) are introduced as scale factors to the SM expected cross section. A two dimensional fit is performed for the two signal strength modifiers assuming a mass hypothesis of $m_H = 125.8\,\mathrm{GeV}$. The likelihood is profiled for all nuisance parameters and a 68% CL is reported by varying the likelihood by $2\Delta \ln \mathcal{L} = 2.3$. Figure 11 (right) shows the result of the (μ_V, μ_F) fit leading to the measurements

$$\mu_V = 1.0^{+2.4}_{-2.3}\,, \tag{3}$$

$$\mu_F = 0.9^{+0.5}_{-0.4}\,. \tag{4}$$

The measured values are consistent with the expectations from the production of a SM Higgs boson.

6.3 Spin-parity measurements

It is crucial to determine the spin and quantum numbers of the new boson. We follow a similar methodology with a kinematic discriminant which includes the description of the interference of identical leptons in the $4e$ and 4μ final states, as discussed in Sec. 4, but instead of the signal-to-background probability ratio we construct the probability ratio for two signal hypotheses. The kinematics of the Higgs or exotic boson decay to the ZZ final state is sensitive to its spin and properties [39, 72–84]. The full-case study has been presented in Refs. [39, 83]. The separation of the SM Higgs boson model and the pseudoscalar (0^-) or minimal coupling spin-2 resonance produced in gluon fusion (2^+_{mgg}) has been presented by CMS [12], with data strongly disfavouring the pure pseudoscalar hypothesis. We expand here the analysis and test new spin-parity hypotheses with respect to those covered in Ref. [12] and consider the models $J^P = 0^+, 0^+_h, 0^-, 2^+_{mgg}, 2^+_{mq\bar{q}}, 1^-, 1^+$, as detailed in Table 3.

Table 3: List of models used in analysis of spin-parity hypotheses corresponding to the pure states of the type noted. The expected separation is quoted for two scenarios, when the signal strength for each hypothesis is pre-determined from the fit to data and when events are generated with SM expectation for the signal yield (μ=1). The observed separation quotes consistency of the observation with the 0^+ model or J^P model, and corresponds to the scenario when the signal strength is pre-determined from the fit to data. The last column quotes CL_s criterion for the J^P model.

J^P	production	comment	expect (μ=1)	obs. 0^+	obs. J^P	CL_s
0^-	$gg \to X$	pseudoscalar	2.6σ (2.8σ)	0.5σ	3.3σ	0.16%
0^+_h	$gg \to X$	higher dim operators	1.7σ (1.8σ)	0.0σ	1.7σ	8.1%
2^+_{mgg}	$gg \to X$	minimal couplings	1.8σ (1.9σ)	0.8σ	2.7σ	1.5%
$2^+_{mq\bar{q}}$	$q\bar{q} \to X$	minimal couplings	1.7σ (1.9σ)	1.8σ	4.0σ	<0.1%
1^-	$q\bar{q} \to X$	exotic vector	2.8σ (3.1σ)	1.4σ	>4.0σ	<0.1%
1^+	$q\bar{q} \to X$	exotic pseudovector	2.3σ (2.6σ)	1.7σ	>4.0σ	<0.1%

The discriminant for signal hypothesis testing is constructed using the matrix element likelihood approach discussed in Section 4 as follows

$$\mathcal{D}_{J^P} = \frac{\mathcal{P}_{\mathrm{SM}}}{\mathcal{P}_{\mathrm{SM}} + \mathcal{P}_{J^P}} = \left[1 + \frac{\mathcal{P}_{J^P}(m_{Z_1}, m_{Z_2}, \vec{\Omega}|m_{4\ell})}{\mathcal{P}_{\mathrm{SM}}(m_{Z_1}, m_{Z_2}, \vec{\Omega}|m_{4\ell})} \right]^{-1}, \tag{5}$$

where $\mathcal{P}_{\mathrm{SM}}$ is the probability distribution for the SM Higgs boson hypothesis, $\mathcal{P}_{J^P}$ is the probability for an alternative model. As input we use the same kinematic observables as discussed in Section 4, invariant masses m_{Z_1}, m_{Z_2} and angles $\vec{\Omega}$.

In addition to simple hypothesis testing, we perform a fit for a continuous parameter which we define as f_{a3} below. The most general decay amplitude for a spin-zero boson can be defined as

$$A = v^{-1}\epsilon_1^{*\mu}\epsilon_2^{*\nu}\left(a_1 g_{\mu\nu} m_H^2 + a_2\, q_\mu q_\nu + a_3 \epsilon_{\mu\nu\alpha\beta}\, q_1^\alpha q_2^\beta\right) = A_1 + A_2 + A_3\,, \quad (6)$$

where ϵ_i are the Z boson polarization vectors, q_i are their momenta, and $q = q_1 + q_2$ is the four-momentum of the spin-zero boson. The SM Higgs boson decay is dominated by the A_1 amplitude, while the $J^P = 0^-$ state decay is expected to be dominated by the A_3 amplitude. The $\mathcal{D}_{0^-}$ discriminant is therefore optimal for the discrimination between the $|A_1|^2$ and $|A_3|^2$ amplitude contributions, while we find their potential interference to have negligible effect on the discriminant distribution or the overall yield of events. We define the parameter $f_{a3} = |A_3|^2/(|A_1|^2 + |A_3|^2)$. Here we neglect the $|A_2|^2$ contribution in order to test the presence of the A_3 amplitude; both are expected to be small or negligible in the SM. The presence of both A_3 and A_1 in decays of one particle would indicate *CP* violation. This f_{a3} parameter allows us to provide a consistency test of the $f_{a3} = 0$ and $f_{a3} = 1$ scenarios, as well as to consider the contribution of both amplitudes in the decay. However, we would like to stress that f_{a3} is not a parameter which defines the mixture of parity-even and parity-odd states. The latter would require a model-dependent interpretation of the f_{a3} measurement.

The statistical analysis remains similar to the Higgs boson search described earlier where we perform the unbinned likelihood fit of the ensemble of selected events, except that instead of the kinematic discriminant for signal-to-background separation, we use the above kinematic discriminant $\mathcal{D}_{J^P}$ for the separation between two signal hypotheses. The second observable combines the $m_{4\ell}$ probability together with the kinematic probability of the angular and mass distributions as used in the K_D calculation, $\mathcal{D}_{\text{bkg}} = \mathcal{P}_{\text{sig}}/(\mathcal{P}_{\text{sig}} + \mathcal{P}_{\text{bkg}})$, where the probabilities $\mathcal{P}$ also include the $m_{4\ell}$ parameterizations for $m_H = 126$ GeV. The analysis of the $\mathcal{D}_{\text{bkg}}$ discriminant is statistically equivalent to the 2D analysis of the $m_{4\ell}$ and K_D distributions. The spin-parity hypothesis analysis is a 2D analysis of the $(\mathcal{D}_{\text{bkg}}, \mathcal{D}_{J^P})$ distributions where correlations of observables are included in the probability parameterizations. In the Figs. 12 and 13 the $\mathcal{D}_{\text{bkg}}$ and $\mathcal{D}_{J^P}$ distributions are shown in the mass range $106 < m_{4\ell} < 141\,\text{GeV}$ used to perform this measurement. The $\mathcal{D}_{\text{bkg}}$ distributions are very similar between the SM and alternative hypotheses but differ significantly from background. The $\mathcal{D}_{J^P}$ distributions provide most discrimination between the two signal hypotheses.

The distribution of $q = -2\ln(\mathcal{L}_{J^P}/\mathcal{L}_{\text{SM}})$ is examined with generated samples of background and signal of seven types (SM 0^+ and six J^P) for $m_H = 126$ GeV. Here the likelihoods $\mathcal{L}$ are calculated with the signal rates allowed to float independently for each signal type and the nuisance parameters are treated as independent. We adjust the relative expected yield distributions in the different channels in alternative J^P hypotheses which differ from SM due to kinematics and detector effects. The expected distributions are generated with the cross section for each type of signal determined from the fit to data. We find consistent results when the expected distributions are generated with the signal event yields according to SM expectation. In Figs. 12 and 13 we show distribution of the $\mathcal{D}_{\text{bkg}}$ and $\mathcal{D}_{J^P}$ observables for the seven hypotheses discussed above $J^P = 0^+, 0_h^+, 0^-, 2_{mgg}^+, 2_{mq\bar{q}}^+, 1^-, 1^+$.

The expected and observed values of $q = -2\ln(\mathcal{L}_{J^P}/\mathcal{L}_{\text{SM}})$ are shown in Fig. 14 and results are summarized in Table 3. We define a CL_s criterion as the ratio of the probabilities to observe, under the J^P and 0^+hypotheses, a value of the test statistics q equal or larger than the one in the data. The data disfavours the alternative hypotheses J^P with a CL_s value in the range 0.1–10%. Figure 12 (right) shows the distribution of $-2\ln\mathcal{L}$ as a function of f_{a3}. The measurement of the fraction of a *CP*-violating contribution to the decay amplitude expressed through the fraction of the corresponding decay rate is $f_{a3} = 0.00^{+0.23}_{-0.00}$ or equivalently $f_{a3} < 0.58$ at 95% CL. The coverage has also been tested with the Feldman-Cousins approach and the results are found consistent. These results confirm our earlier measurements [12] with improved precision and expand on the number of models tested. The results presented in Table 3 show an observed deviation from an average expectation for an alternative hypothesis of 4σ or greater in three cases, $2^+_{mq\bar{q}}$, 1^+, and 1^-. In these three cases the deviation from the mean expectation of the SM ranges from 1.4 to 1.8σ. Strong correlations, seen in both data and simulation, are found between the D_{J^P} values of these different hypotheses. One of the features leading to such correlation is the distribution of the invariant masses m_{Z_1} and m_{Z_2}, with somewhat more off-shell events observed than expected on average in the SM.

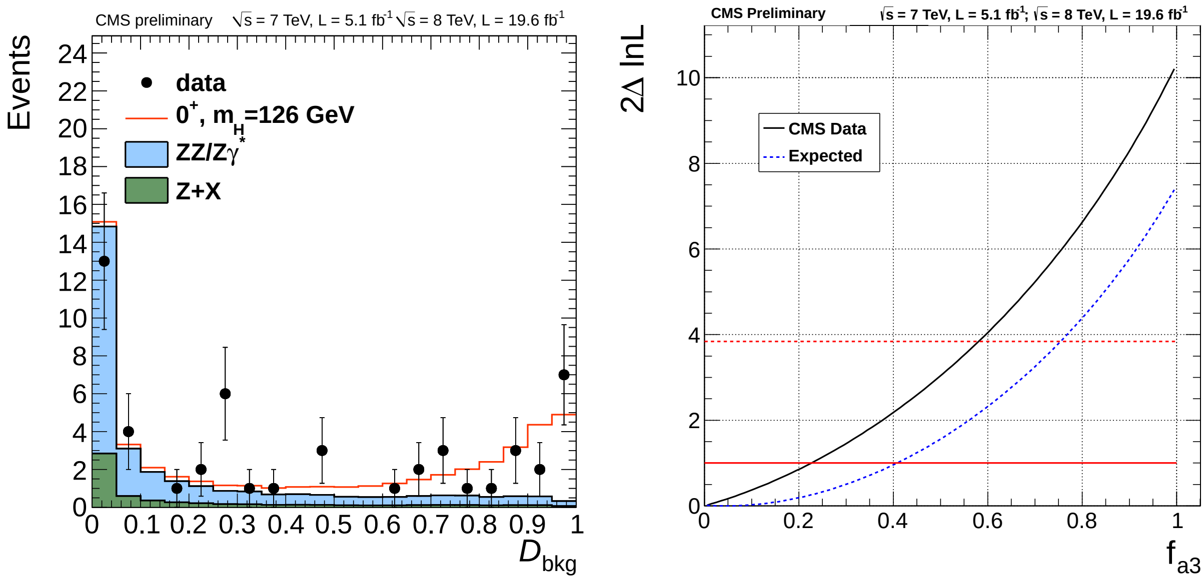

Figure 12: Distribution of $\mathcal{D}_{\rm bkg}$ in data and MC expectations for the background and for a signal resonance consistent with SM Higgs boson at $m_H = 126$ GeV (left). Average expected and observed distribution of $-2\ln\mathcal{L}$ as a function of f_{a3} (right).

7 Summary

In summary, a study of the standard model Higgs boson has been presented in the four-lepton decay modes, $\mathrm{H} \to \mathrm{ZZ} \to 4\ell$ and $\mathrm{H} \to \mathrm{ZZ} \to 2\ell 2\tau$. The mass distributions are measured with four-lepton invariant masses $m_{4\ell}$ or $m_{2\ell 2\tau} > 100\,\mathrm{GeV}$ using 5.1 fb^{-1} at $\sqrt{s} = 7$ TeV and 19.6 fb^{-1} at $\sqrt{s} = 8$ TeV. The measurements use for each event the information from the measured four-lepton mass, the mass uncertainty, a kinematic discriminant, and information sensitive to the production mechanism, such as associated di-jet characteristics and transverse momentum of the four-lepton system. Upper limits at 95% confidence level exclude the SM-like Higgs boson in the range 130–827 GeV while the expected exclusion range is 113.5–778 GeV. The new boson discovered by the CMS and ATLAS experiments is observed in the 4ℓ channel, with a local significance of 6.7 standard deviations above the expected background. A measurement of its mass gives 125.8 ± 0.5 (stat.) ± 0.2 (syst.) GeV. The signal strength μ, relative to the expectation for the standard model Higgs boson, is measured to be $\mu = 0.91^{+0.30}_{-0.24}$ at the measured mass. The signal strength modifiers associated with vector bosons and fermions in production are measured to be $\mu_V = 1.0^{+2.4}_{-2.3}$ and $\mu_F = 0.9^{+0.5}_{-0.4}$, thus consistent with the SM expectations.

The spin-parity of the boson is studied and the pure scalar hypothesis is found to be consistent with the observation when compared to six other spin-parity hypotheses. The fraction of a CP-violating contribution to the decay amplitude, expressed through the fraction f_{a3} of the corresponding decay rate, is measured to be $f_{a3} = 0.00^{+0.23}_{-0.00}$, and thus consistent with the SM expectation. The data disfavour the pure pseudoscalar hypothesis 0^- with a $\mathrm{CL_s}$ value of 0.16%, and disfavour the pure spin-2 hypothesis of a narrow resonance with minimal couplings to the vector bosons with a $\mathrm{CL_s}$ value of 1.5%. The spin-1 hypotheses are disfavoured with an even higher confidence.

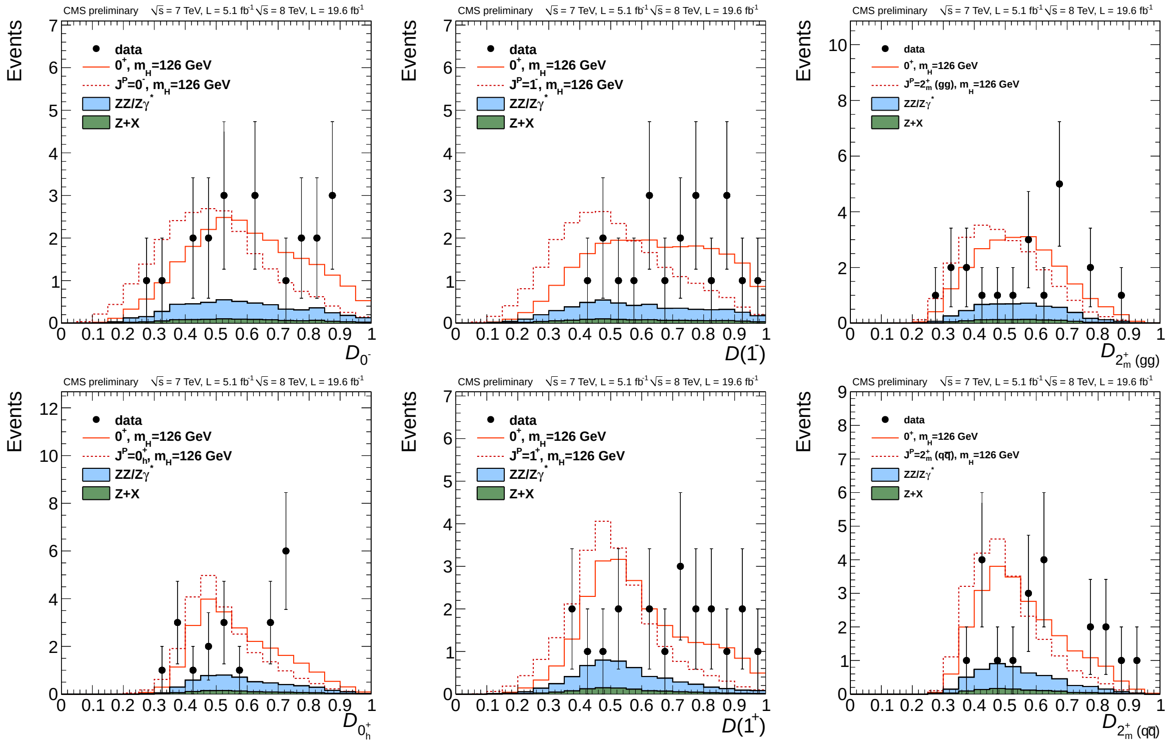

Figure 13: Distributions of $\mathcal{D}_{J^P}$ with a requirement $\mathcal{D}_{\rm bkg} > 0.5$. Distributions in data (points with error bars) and expectations for background and signal are shown. Six alternative hypotheses are tested from top to bottom and left to right: $J^P = 0^-, 0^+_h, 1^-, 1^+, 2^+_m(gg), 2^+_m(q\bar{q})$.

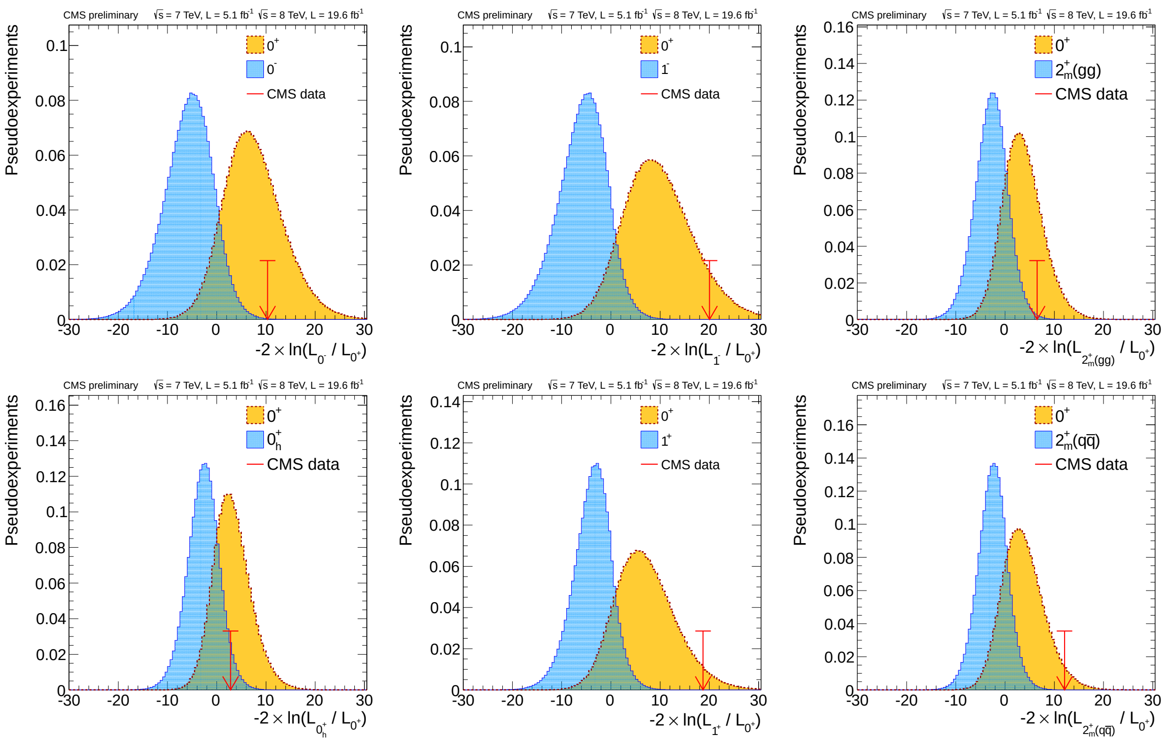

Figure 14: Distribution of $q = -2\ln(\mathcal{L}_{J^P}/\mathcal{L}_{\rm SM})$ for two signal types (0^+ represented by the yellow histogram and alternative J^P hypothesis by the blue histogram) for $m_H = 126$ GeV shown with a large number of generated experiments. The arrow indicates the observed value. Six alternative hypotheses are tested from top to bottom and left to right: $J^P = 0^-, 0^+_h, 1^-, 1^+, 2^+_{mgg}, 2^+_{mq\bar{q}}$.

References

[1] S. L. Glashow, "Partial Symmetries of Weak Interactions", *Nucl. Phys.* **22** (1961) 579, doi:10.1016/0029-5582(61)90469-2.

[2] S. Weinberg, "A Model of Leptons", *Phys. Rev. Lett.* **19** (1967) 1264, doi:10.1103/PhysRevLett.19.1264.

[3] A. Salam, "Weak and electromagnetic interactions", in *Elementary particle physics: relativistic groups and analyticity*, N. Svartholm, ed., p. 367. Almquvist & Wiskell, 1968. Proceedings of the eighth Nobel symposium.

[4] F. Englert and R. Brout, "Broken Symmetry and the Mass of Gauge Vector Mesons", *Phys. Rev. Lett.* **13** (1964) 321, doi:10.1103/PhysRevLett.13.321.

[5] P. W. Higgs, "Broken symmetries, massless particles and gauge fields", *Phys. Lett.* **12** (1964) 132, doi:10.1016/0031-9163(64)91136-9.

[6] P. W. Higgs, "Broken Symmetries and the Masses of Gauge Bosons", *Phys. Rev. Lett.* **13** (1964) 508, doi:10.1103/PhysRevLett.13.508.

[7] G. S. Guralnik, C. R. Hagen, and T. W. B. Kibble, "Global Conservation Laws and Massless Particles", *Phys. Rev. Lett.* **13** (1964) 585, doi:10.1103/PhysRevLett.13.585.

[8] P. W. Higgs, "Spontaneous Symmetry Breakdown without Massless Bosons", *Phys. Rev.* **145** (1966) 1156, doi:10.1103/PhysRev.145.1156.

[9] T. W. B. Kibble, "Symmetry breaking in non-Abelian gauge theories", *Phys. Rev.* **155** (1967) 1554, doi:10.1103/PhysRev.155.1554.

[10] CMS Collaboration, "Observation of a new boson at a mass of 125 GeV with the CMS experiment at the LHC", *Phys. Lett. B* **716** (2012) 30–61, doi:10.1016/j.physletb.2012.08.021, arXiv:1207.7235.

[11] ATLAS Collaboration, "Observation of a new particle in the search for the Standard Model Higgs boson with the ATLAS detector at the LHC", *Phys. Lett. B* **716** (2012) 1–29, doi:10.1016/j.physletb.2012.08.020, arXiv:1207.7214.

[12] CMS Collaboration, "Study of the Mass and Spin-Parity of the Higgs Boson Candidate via Its Decays to Z Boson Pairs", *Phys. Rev. Lett.* **110** (2013) 081803, doi:10.1103/PhysRevLett.110.081803, arXiv:1212.6639.

[13] ATLAS Collaboration, "Search for the Standard Model Higgs boson in the decay channel $H \to$ ZZ(*) $\to 4\ell$ with 4.8 fb-1 of pp collision data at $\sqrt{s} = 7$ TeV with ATLAS", *Phys. Lett. B* **710** (2012) 383–402, doi:10.1016/j.physletb.2012.03.005, arXiv:1202.1415.

[14] CMS Collaboration, "Search for the standard model Higgs boson in the decay channel H to ZZ to 4 leptons in pp collisions at sqrt(s) = 7 TeV", *Phys. Rev. Lett.* **108** (2012) 111804, doi:10.1103/PhysRevLett.108.111804, arXiv:1202.1997.

[15] CMS Collaboration, "Search for the standard model Higgs boson in the H to ZZ to ll to $\tau\tau$ decay channel in pp collisions at $\sqrt{s} = 7\,$TeV", *JHEP* **1203** (2012) 081, arXiv:1202.3617.

[16] CMS Collaboration, "Combined results of searches for the standard model Higgs boson in pp collisions at sqrt(s) = 7 TeV", *Phys. Lett. B* **710** (2012) 26–48, doi:10.1016/j.physletb.2012.02.064, arXiv:1202.1488.

[17] ATLAS Collaboration, "Combined search for the Standard Model Higgs boson using up to 4.9 fb^{-1} of pp collision data at $\sqrt{s} = 7$ TeV with the ATLAS detector at the LHC", *Phys. Lett. B* **710** (2012) 49–66, doi:10.1016/j.physletb.2012.02.044, arXiv:1202.1408.

[18] ATLAS Collaboration, "Combined search for the Standard Model Higgs boson in pp collisions at sqrt(s) = 7 TeV with the ATLAS detector", *Phys. Rev. D* **86** (2012) 032003, doi:10.1103/PhysRevD.86.032003, arXiv:1207.0319.

[19] ALEPH, DELPHI, L3, OPAL Collaborations, and the LEP Working Group for Higgs boson searches, "Search for the standard model Higgs boson at LEP", *Phys. Lett. B* **565** (2003) 61, doi:10.1016/S0370-2693(03)00614-2, arXiv:hep-ex/0306033.

[20] CMS Collaboration, "Observation of Z decays to four leptons with the CMS detector at the LHC", *JHEP* **1212** (2012) 034, doi:10.1007/JHEP12(2012)034, arXiv:1210.3844.

[21] CMS Collaboration, "Updated results on the new boson discovered in the search for the standard model Higgs boson in the $\mathrm{H} \to \mathrm{ZZ} \to 4\ell$ channel in pp collisions at $\sqrt{s} = 7$ and 8 TeV", CMS Physics Analysis Summary CMS-PAS-HIG-12-041, (2012).

[22] CMS Collaboration, "The CMS experiment at the CERN LHC", *JINST* **3** (2008) S08004, doi:10.1088/1748-0221/3/08/S08004.

[23] CMS Collaboration, "Particle-Flow Event Reconstruction in CMS and Performance for Jets, Taus, and MET", CMS Physics Analysis Summary CMS-PAS-PFT-09-001, (2009).

[24] CMS Collaboration, "Commissioning of the Particle–Flow reconstruction in Minimum–Bias and Jet Events from pp Collisions at 7 TeV", CMS Physics Analysis Summary CMS-PAS-PFT-10-002, (2010).

[25] S. Baffioni et al., "Electron reconstruction in CMS", *Eur. Phys. J. C* **49** (2007) 1099, doi:10.1140/epjc/s10052-006-0175-5.

[26] CMS Collaboration, "Electron reconstruction and identification at $\sqrt{s} = 7$ TeV", CMS Physics Analysis Summary CMS-PAS-EGM-10-004, (2010).

[27] CMS Collaboration, "Electron commissioning results at $\sqrt{s} = 7$ TeV", CMS Detector Performance Summary CMS-DP-2011-003, (2011).

[28] CMS Collaboration, "Electron performance with 19.6 fb^{-1} of data at $\sqrt{s} = 8$ TeV with the CMS detector", CMS Detector Performance Summary CMS-DP-2013-003, (2013).

[29] CMS Collaboration, "Performance of CMS muon reconstruction in pp collision events at sqrt(s) = 7 TeV", *JINST* **7** (2012) P10002, doi:10.1088/1748-0221/7/10/P10002, arXiv:1206.4071.

[30] CMS Collaboration, "Commissioning of the particle-flow event reconstruction with leptons from J/ψ and W decays at 7 TeV", CMS Physics Analysis Summary CMS-PAS-PFT-10-003, (2010).

[31] CMS Collaboration, “Performance of tau-lepton reconstruction and identification in CMS”, *JINST* **7** (2012) P01001, doi:10.1088/1748-0221/7/01/P01001, arXiv:1109.6034.

[32] M. Cacciari and G. P. Salam and G. Soyez, “The anti-k_t jet clustering algorithm”, *JHEP* **04** (2008) 063, doi:10.1088/1126-6708/2008/04/063, arXiv:0802.1189.

[33] M. Cacciari, G. P. Salam, G. Soyez, “FastJet user manual”, (2011). arXiv:hep-ph/1111.6097v1.

[34] M. Cacciari, G. P. Salam, “Dispelling the N^3 myth for the k_t jet-finder”, *Phys. Lett. B* **641** (2006) 57, doi:10.1016/j.physletb.2006.08.037, arXiv:hep-ph/0512210.

[35] CMS Collaboration, “Determination of Jet Energy Calibration and Transverse Momentum Resolution in CMS”, *JINST* **6** (2011) 11002, doi:10.1088/1748-0221/6/11/P11002.

[36] M. Cacciari and G. P. Salam, “Pileup subtraction using jet areas”, *Phys. Lett. B* **659** (2008) 119, doi:10.1016/j.physletb.2007.09.077, arXiv:0707.1378.

[37] CMS Collaboration, “Measurement of the Inclusive W and Z Production Cross Sections in pp Collisions at $\sqrt{s} = 7\,\mathrm{TeV}$”, *JHEP* **10** (2011) 132, doi:10.1007/JHEP10(2011)132.

[38] S. Frixione, P. Nason, and C. Oleari, “Matching NLO QCD computations with Parton Shower simulations: the POWHEG method”, *JHEP* **11** (2007) 070, doi:10.1088/1126-6708/2007/11/070, arXiv:0709.2092.

[39] Y. Gao et al., “Spin determination of single-produced resonances at hadron colliders”, *Phys. Rev. D* **81** (2010) 075022, doi:10.1103/PhysRevD.81.075022, arXiv:1001.3396.

[40] G. Passarino, C. Sturm, and S. Uccirati, “Higgs Pseudo-Observables, Second Riemann Sheet and All That”, *Nucl. Phys. B* **834** (2010) 77, doi:10.1016/j.nuclphysb.2010.03.013, arXiv:1001.3360.

[41] S. Goria, G. Passarino, and D. Rosco, “The Higgs Boson Lineshape”, *Nucl. Phys. B* **864** (2012) 530–579, doi:10.1016/j.nuclphysb.2012.07.006, arXiv:1112.5517.

[42] N. Kauer and G. Passarino, “Inadequacy of zero-width approximation for a light Higgs boson signal”, *JHEP* **1208** (2012) 116, doi:10.1007/JHEP08(2012)116, arXiv:1206.4803.

[43] G. Passarino, “Higgs Interference Effects in gg $\to$ ZZ and their Uncertainty”, *JHEP* **1208** (2012) 146, doi:10.1007/JHEP08(2012)146, arXiv:1206.3824.

[44] N. Kauer, “Signal-background interference in gg$\to$H$\to$VV”, arXiv:1201.1667.

[45] T. Sjöstrand, S. Mrenna, and P. Z. Skands, “PYTHIA 6.4 Physics and Manual”, *JHEP* **05** (2006) 026, doi:10.1088/1126-6708/2006/05/026, arXiv:hep-ph/0603175.

[46] C. Anastasiou, R. Boughezal, and F. Petriello, “Mixed QCD-electroweak corrections to Higgs boson production in gluon fusion”, *JHEP* **04** (2009) 003, doi:10.1088/1126-6708/2009/04/003, arXiv:0811.3458.

[47] D. de Florian and M. Grazzini, "Higgs production through gluon fusion: updated cross sections at the Tevatron and the LHC", *Phys. Lett. B* **674** (2009) 291, doi:10.1016/j.physletb.2009.03.033, arXiv:0901.2427.

[48] J. Baglio and A. Djouadi, "Higgs production at the LHC", *JHEP* **03** (2011) 055, doi:10.1007/JHEP03(2011)055, arXiv:1012.0530.

[49] LHC Higgs Cross Section Working Group, "Handbook of LHC Higgs Cross Sections: 1. Inclusive Observables", CERN Report CERN-2011-002, (2011).

[50] A. Djouadi, M. Spira, and P. M. Zerwas, "Production of Higgs bosons in proton colliders: QCD corrections", *Phys. Lett. B* **264** (1991) 440–446, doi:10.1016/0370-2693(91)90375-Z.

[51] S. Dawson, "Radiative corrections to Higgs boson production", *Nucl. Phys. B* **359** (1991) 283, doi:10.1016/0550-3213(91)90061-2.

[52] M. Spira et al., "Higgs boson production at the LHC", *Nucl. Phys. B* **453** (1995) 17, doi:10.1016/0550-3213(95)00379-7, arXiv:hep-ph/9504378.

[53] R. V. Harlander and W. B. Kilgore, "Next-to-next-to-leading order Higgs production at hadron colliders", *Phys. Rev. Lett.* **88** (2002) 201801, doi:10.1103/PhysRevLett.88.201801, arXiv:hep-ph/0201206.

[54] C. Anastasiou and K. Melnikov, "Higgs boson production at hadron colliders in NNLO QCD", *Nucl. Phys. B* **646** (2002) 220, doi:10.1016/S0550-3213(02)00837-4, arXiv:hep-ph/0207004.

[55] V. Ravindran, J. Smith, and W. L. van Neerven, "NNLO corrections to the total cross section for Higgs boson production in hadron-hadron collisions", *Nucl. Phys. B* **665** (2003) 325, doi:10.1016/S0550-3213(03)00457-7, arXiv:hep-ph/0302135.

[56] S. Catani et al., "Soft-gluon resummation for Higgs boson production at hadron colliders", *JHEP* **07** (2003) 028, doi:10.1088/1126-6708/2003/07/028, arXiv:hep-ph/0306211.

[57] S. Actis et al., "NLO Electroweak Corrections to Higgs Boson Production at Hadron Colliders", *Phys. Lett. B* **670** (2008) 12, doi:10.1016/j.physletb.2008.10.018, arXiv:0809.1301.

[58] M. Ciccolini, A. Denner, and S. Dittmaier, "Strong and electroweak corrections to the production of Higgs + 2-jets via weak interactions at the LHC", *Phys. Rev. Lett.* **99** (2007) 161803, doi:10.1103/PhysRevLett.99.161803, arXiv:0707.0381.

[59] M. Ciccolini, A. Denner, and S. Dittmaier, "Electroweak and QCD corrections to Higgs production via vector-boson fusion at the LHC", *Phys. Rev. D* **77** (2008) 013002, doi:10.1103/PhysRevD.77.013002, arXiv:0710.4749.

[60] T. Figy, C. Oleari, and D. Zeppenfeld, "Next-to-leading order jet distributions for Higgs boson production via weak-boson fusion", *Phys. Rev. D* **68** (2003) 073005, doi:10.1103/PhysRevD.68.073005, arXiv:hep-ph/0306109.

[61] K. Arnold et al., "VBFNLO: A parton level Monte Carlo for processes with electroweak bosons", *Comput. Phys. Commun.* **180** (2009) 1661, doi:10.1016/j.cpc.2009.03.006, arXiv:0811.4559.

[62] P. Bolzoni et al., "Higgs production via vector-boson fusion at NNLO in QCD", *Phys. Rev. Lett.* **105** (2010) 011801, doi:10.1103/PhysRevLett.105.011801, arXiv:1003.4451.

[63] A. Bredenstein et al., "Precise predictions for the Higgs-boson decay H → WW/ZZ → 4 leptons", *Phys. Rev. D* **74** (2006) 013004, doi:10.1103/PhysRevD.74.013004, arXiv:hep-ph/0604011.

[64] A. Bredenstein et al., "Radiative corrections to the semileptonic and hadronic Higgs-boson decays H →W W / Z Z→ 4 fermions", *JHEP* **02** (2007) 080, doi:10.1088/1126-6708/2007/02/080, arXiv:hep-ph/0611234.

[65] A. Djouadi, J. Kalinowski, and M. Spira, "HDECAY: A program for Higgs boson decays in the standard model and its supersymmetric extension", *Comput. Phys. Commun.* **108** (1998) 56, doi:10.1016/S0010-4655(97)00123-9, arXiv:hep-ph/9704448.

[66] S. Actis et al., "NNLO Computational Techniques: the Cases $H \to \gamma\gamma$ and $H \to gg$", *Nucl. Phys. B* **811** (2009) 182, doi:10.1016/j.nuclphysb.2008.11.024, arXiv:0809.3667.

[67] J. Alwall et al., "MadGraph/MadEvent v4: The New Web Generation", *JHEP* **09** (2007) 028, doi:10.1088/1126-6708/2007/09/028, arXiv:0706.2334.

[68] T. Binoth, N. Kauer, and P. Mertsch, "Gluon-induced QCD corrections to $pp \to ZZ \to \ell\bar{\ell}\ell'\bar{\ell}'$", in *Proceedings of the XVI Int. Workshop on Deep-Inelastic Scattering and Related Topics (DIS'07)*. 2008. arXiv:0807.0024. doi:10.3360/dis.2008.142.

[69] H.-L. Lai et al., "Uncertainty induced by QCD coupling in the CTEQ global analysis of parton distributions", *Phys. Rev. D* **82** (2010) 054021, doi:10.1103/PhysRevD.82.054021, arXiv:1004.4624.

[70] H.-L. Lai et al., "New parton distributions for collider physics", *Phys. Rev. D* **82** (2010) 074024, doi:10.1103/PhysRevD.82.074024, arXiv:1007.2241.

[71] J. Allison et al., "Geant4 developments and applications", *IEEE Trans. Nucl. Sci.* **53** (2006) 270, doi:10.1109/TNS.2006.869826.

[72] A. Soni and R. Xu, "Probing CP violation via Higgs decays to four leptons", *Phys. Rev. D* **48** (1993) 5259–5263, doi:10.1103/PhysRevD.48.5259, arXiv:hep-ph/9301225.

[73] V. D. Barger et al., "Higgs bosons: Intermediate mass range at e+ e- colliders", *Phys. Rev. D* **49** (1994) 79–90, doi:10.1103/PhysRevD.49.79, arXiv:hep-ph/9306270.

[74] S. Y. Choi et al., "Identifying the Higgs spin and parity in decays to Z pairs", *Phys. Lett. B* **553** (2003) 61–71, doi:10.1016/S0370-2693(02)03191-X, arXiv:hep-ph/0210077.

[75] B. Allanach et al., "Exploring small extra dimensions at the large hadron collider", *JHEP* **0212** (2002) 039, arXiv:hep-ph/0211205.

[76] C. P. Buszello et al., "Prospective analysis of spin- and CP-sensitive variables in $H \to ZZ \to l(1)^+l(1)^-l(2)^+l(2)^-$ at the LHC", *Eur. Phys. J. C* **32** (2004) 209–219, doi:10.1140/epjc/s2003-01392-0, arXiv:hep-ph/0212396.

[77] R. M. Godbole, D. J. Miller, and M. M. Muhlleitner, "Aspects of CP violation in the H ZZ coupling at the LHC", *JHEP* **0712** (2007) 031, doi:10.1088/1126-6708/2007/12/031, arXiv:0708.0458.

[78] W.-Y. Keung, I. Low, and J. Shu, "Landau-Yang Theorem and Decays of a Z′ Boson into Two Z Bosons", *Phys. Rev. Lett.* **101** (2008) 091802, doi:10.1103/PhysRevLett.101.091802, arXiv:0806.2864.

[79] O. Antipin and A. Soni, "Towards establishing the spin of warped gravitons", *JHEP* **0810** (2008) 018, doi:10.1088/1126-6708/2008/10/018, arXiv:0806.3427.

[80] K. Hagiwara, Q. Li, and K. Mawatari, "Jet angular correlation in vector-boson fusion processes at hadron colliders", *JHEP* **0907** (2009) 101, doi:10.1088/1126-6708/2009/07/101, arXiv:0905.4314.

[81] A. De Rujula et al., "Higgs look-alikes at the LHC", *Phys. Rev. D* **82** (2010) 013003, doi:10.1103/PhysRevD.82.013003, arXiv:1001.5300.

[82] J. S. Gainer et al., "Improving the sensitivity of Higgs boson searches in the golden channel", *JHEP* **1111** (2011) 027, doi:10.1007/JHEP11(2011)027, arXiv:1108.2274.

[83] S. Bolognesi et al., "On the spin and parity of a single-produced resonance at the LHC", *Phys. Rev. D* **86** (2012) 095031, doi:10.1103/PhysRevD.86.095031, arXiv:1208.4018.

[84] Y. Chen, N. Tran, and R. Vega-Morales, "Scrutinizing the Higgs Signal and Background in the $2e2\mu$ Golden Channel", arXiv:1211.1959.

[85] J. M. Campbell and R. K. Ellis, "MCFM for the Tevatron and the LHC", *Nucl. Phys. Proc. Suppl.* **205** (2010) 10, doi:10.1016/j.nuclphysbps.2010.08.011, arXiv:1007.3492.

[86] J. M. Campbell and R. K. Ellis, "An update on vector boson pair production at hadron colliders", *Phys. Rev. D* **60** (1999) 113006, doi:10.1103/PhysRevD.60.113006, arXiv:hep-ph/9905386.

[87] J. M. Campbell, R. Ellis, and C. Williams, "Vector boson pair production at the LHC", *JHEP* **07** (2011) 018, doi:10.1007/JHEP07(2011)018, arXiv:1105.0020.

[88] P. Avery et al., "Precision studies of the Higgs boson decay channel H $\to$ ZZ* $\to$ 4l with MEKD", *accepted by Phys.Rev.D.* (2012) arXiv:1210.0896.

[89] M. Botje et al., "The PDF4LHC Working Group Interim Recommendations", (2011). arXiv:1101.0538.

[90] S. Alekhin et al., "The PDF4LHC Working Group Interim Report", (2011). arXiv:1101.0536.

[91] H.-L. Lai et al., "New parton distributions for collider physics", *Phys. Rev. D* **82** (2010) 074024, doi:10.1103/PhysRevD.82.074024, arXiv:1007.2241.

[92] A. Martin et al., "Parton distributions for the LHC", *Eur. Phys. J. C* **63** (2009) 189, doi:10.1140/epjc/s10052-009-1072-5, arXiv:0901.0002.

[93] R. D. Ball et al., “Impact of Heavy Quark Masses on Parton Distributions and LHC Phenomenology”, *Nucl. Phys. B* **849** (2011) 296, doi:10.1016/j.nuclphysb.2011.03.021, arXiv:1101.1300.

[94] CMS Collaboration, “Absolute Calibration of the CMS Luminosity Measurement: Summer 2011 Update”, CMS Physics Analysis Summary CMS-PAS-EWK-11-001, (2011).

[95] ATLAS and CMS Collaborations, LHC Higgs Combination Group, “Procedure for the LHC Higgs boson search combination in Summer 2011”, ATL-PHYS-PUB/CMS NOTE 2011-11, 2011/005, (2011).

[96] T. Junk, “Confidence level computation for combining searches with small statistics”, *Nucl. Instrum. Meth. A* **434** (1999) 435, doi:10.1016/S0168-9002(99)00498-2, arXiv:hep-ex/9902006.

[97] A. Read, “Modified frequentist analysis of search results (the CL_s method)”, Technical Report CERN-OPEN-2000-005, CERN, (2000).

[98] Particle Data Group, “Review of particle physics”, *J. Phys. G* **37** (2010) 075021, doi:10.1088/0954-3899/37/7A/075021.

[99] M. Oreglia, “A study of the reactions $\psi' \to \gamma\gamma\psi$”. PhD thesis, Stanford University, 1980. SLAC-0236.

[100] G. Bozzi et al., “Transverse-momentum resummation and the spectrum of the Higgs boson at the LHC”, *Nucl. Phys. B* **737** (2006) 73, doi:10.1016/j.nuclphysb.2005.12.022, arXiv:hep-ph/0508068.

[101] D. de Florian et al., “Transverse-momentum resummation: Higgs boson production at the Tevatron and the LHC”, *JHEP* **1111** (2011) 064, doi:10.1007/JHEP11(2011)064, arXiv:1109.2109.

[102] G. Bozzi et al., “The q(T) spectrum of the Higgs boson at the LHC in QCD perturbation theory”, *Phys. Lett. B* **564** (2003) 65–72, doi:10.1016/S0370-2693(03)00656-7, arXiv:hep-ph/0302104.

[103] CMS Collaboration, “Electron and photon energy calibration and resolution with the CMS ECAL at $\sqrt{s}$ = 7 TeV”, CMS Physics Analysis Summary CMS-PAS-EGM-11-001, (2013).

[104] CMS Collaboration, “ECAL Performance Plots, 2012 Data”, CMS Detector Performance Summary CMS-DP-2012-015, (2012).

A Appendix: Four-lepton mass scale and resolution

This appendix summarises the procedures used to define and validate the absolute scale of the four-lepton mass and four-lepton mass resolutions assigned to individual events. The described procedure allows us to set the absolute four-lepton mass scale with $0.1 - 0.3\%$ uncertainties, depending on the four-lepton final state ($4e$, 4μ, $2e2\mu$), and ascribe a 20% uncertainty on four-lepton mass resolutions assigned on an event-by-event basis. Using events with individually determined mass resolutions allows us to assign the proper mass error based on the quality of the actually observed events, leading to an average expected improvement of 8% on the measured mass uncertainty.

A.1 Lepton reconstruction, momentum determination and resolution

A.1.1 Electrons

Electron reconstruction

Electron candidates are reconstructed from clusters of energy deposits in the ECAL, which are then matched to tracks reconstructed in the silicon tracker. The energy deposited in the ECAL is measured in clusters of clusters (super-clusters) which collect bremsstrahlung photons emitted in the tracker material. Trajectories, either initiated "outside-in" from ECAL superclusters or "inside-out" from measurements in the innermost tracker layers, are reconstructed using a dedicated modeling of the electron energy loss and fitted with a Gaussian sum filter. Electron classes are defined according to the bremmstrahlung pattern measured in the ECAL and in the tracker as: *golden* (best measurement), *bigbrem* (high amount of bremsstrahlung measured from the tracker), *showering* (bremsstrahlung pattern from the ECAL supercluster), *badtrack* (poor track measurement) and *crack* (electron close to ECAL modules boundaries). More details can be found in [25–28].

Energy measurement

Standard CMS procedures to calibrate the energy response of individual crystals are used [103, 104]. The (raw) energy collected in ECAL superclusters is then corrected for the imperfect containment of the clustering algorithm, losses due to bremsstrahlung and interactions upstream the ECAL and leakage arising from showers near gaps between crystals or between ECAL modules or supermodules. This is done using a regression technique based on a boosted decision tree trained on a Drell-Yan simulated sample. Different set of variables are used depending on whether the electron is detected in the ECAL barrel or in one of the ECAL endcaps. The reconstructed number of vertices in the event as well as the ρ estimate of the average energy density in the event are also included to correct for the pileup contribution. Using this multivariate technique, the resolution is improved by $\sim$10% for electrons from $Z \to e^+e^-$decays compared to a more traditional approach for supercluster corrections based on parametrisations of the energy response from simulation.

Energy calibration

Small residual discrepancies between data and simulation remains in particular due to imperfect corrections at the crystal level of the transparency loss due to irradiation, especially in the forward region. $Z \to e^+e^-$events are used to derive energy scale correction factors which are applied on the data to best match the simulation. This procedure consists in two steps. A first set of corrections is obtained by comparing the Z mass scale in the data and in the simulation as a function of the run period and in different pseudorapidity regions to factorize the transparency loss effect. In a second step corrections are derived using the same pseudorapidity regions but dividing into *showering* and *golden* electrons to further correct for residual discrepancies depending on the bremsstrahlung pattern. The product of these two sets of corrections is applied on the energy obtained from the regression for the data. Correction factors are in general below 0.5% in the central barrel and up to ∼1.5% in the forward part of the ECAL endcaps. In addition, the energy in the simulation is modified applying a random Gaussian multiplicative factor of mean $1 + \Delta E/E$ and width $\Delta\sigma$, where $\Delta E/E$ is the relative energy scale difference $\Delta E/E = (\Delta m_{data} - \Delta m_{MC})/m_Z$ and $\Delta\sigma$ is the relative difference in resolution between data and simulation.

Momentum determination

At high energy the precision is dominated by the ECAL while at low p_T the tracker momentum determination performs better. Moreover for electrons in crack regions or in ECAL regions close to dead channels the measurement accuracy and resolution can also be improved by combining the ECAL energy with the track momentum. The electron momentum magnitude is therefore determined by combining the two estimates, taking the weighted average with the weights determined by their respective errors. For the ECAL measurement, the associated error is obtained from the regression while for the track momentum it is obtained from the track fit. The momentum angles are taken from the fitted track parameters at the closest approach to the nominal beam spot position. Figure 15 presents the expected effective and Gaussian momentum resolution of the combined momentum as a function of the initial electron energy. The expected effective resolution for the ECAL only and tracker only estimates are also shown.

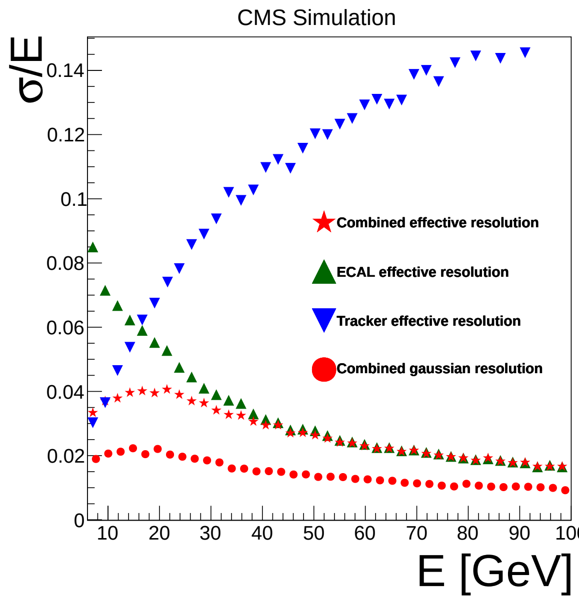

Figure 15: Expected resolution for prompt and isolated electrons in the ECAL barrel as a function of the initial electron energy from the ECAL, the tracker and the combined estimates. The resolution is evaluated as half the minimal width that contains 68.3% of the reconstructed energy or momentum distribution (effective resolution) or using a Gaussian fit of the core of the momentum distribution. The energy from the regression is used for the ECAL measurement.

Electron momentum scale and resolution

The electron momentum scale is validated by comparing the invariant mass distribution of $Z \to e^+e^-$ events in data with the simulation as a function of the electron class. Fits of the

$Z \rightarrow e^+e^-$ line shape are performed using a Breit-Wigner (BW) function convoluted with a Crystal Ball (CB) to model the detector effects. The parameters of the BW function are fixed to the nominal Z mass and natural width. An excellent agreement is found in the ECAL barrel for the mass scale, while in the ECAL endcaps the agreement is slightly less good. No significant dependency of the electron momentum scale with pileup is observed. The above results are dominated by electrons in the transverse momentum range typical of on-shell $Z \rightarrow e^+e^-$ decays. To further assess the momentum scale in the p_T range of off-shell Z boson decays, the mass scale is also measured as function of the electron p_T as presented in Fig. 16 (left). The scale difference is consistent with zero within 0.2% in the p_T range of $\sim$ 35-50 GeV, while a trend is observed of up to $\sim$1.5% when going towards low p_T electrons and in the ECAL endcaps. Results from $J/\Psi \rightarrow e^+e^-$ and $\Upsilon \rightarrow e^+e^-$ events are found consistent with the measurements from $Z \rightarrow e^+e^-$ at low p_T and are also presented on Fig. 16 (left). The measured p_T dependency is propagated to the reconstructed four leptons mass from Higgs events using the simulation and the resulting shift of 0.3% (0.1%) for the 4e (2e2μ) channel is used as systematic on the signal mass scale. The effective di-electron mass resolution, with the contribution from the natural width subtracted, is shown on Fig. 16 (right) for different categories according to the class and pseudorapidity of each electron together with expectation from simulation. The effective instrumental resolution ranges from 1.2% for the best category (both electrons in EB and *golden* or *bigbrem*) to 4% for the worst category (both electrons in EE and *showering* or *crack* or *badtrack*). The data and simulation are in agreement, with a relative difference between data and simulation of less than 10%. Results are presented for the data collected at $\sqrt{s}$ = 8 TeV, similar results are obtained for the data collected at $\sqrt{s}$ = 7 TeV.

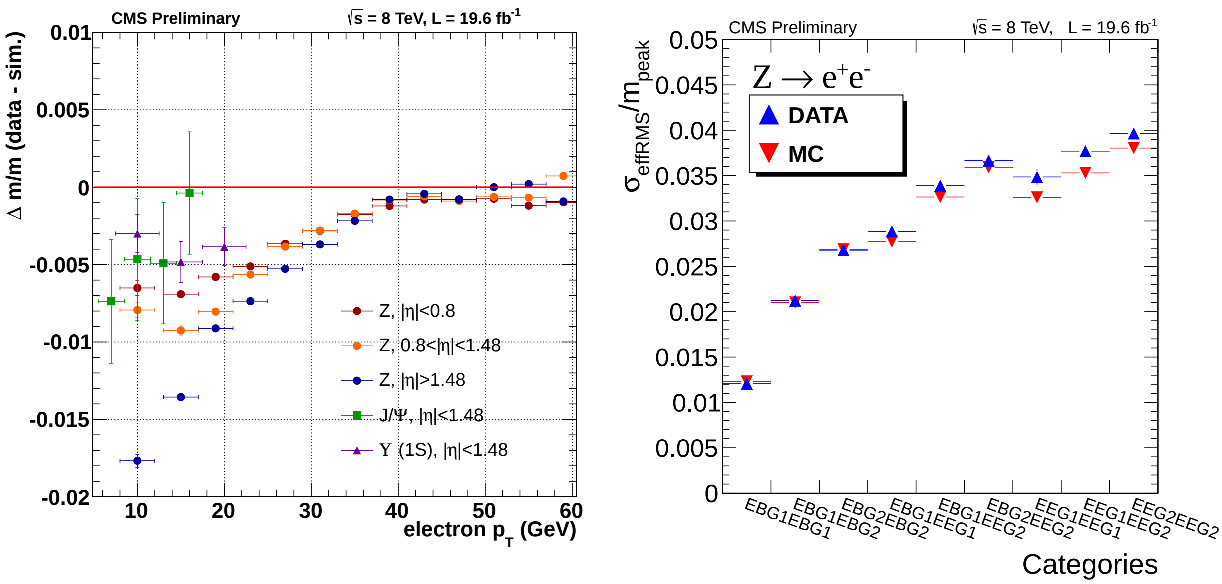

Figure 16: Relative difference between the di-electron mass scale in data and simulation as obtained from $Z \rightarrow e^+e^-$, J/Ψ and Υ events as a function of the electron transverse momentum and for different pseudorapidity regions (left). Instrumental di-electron mass resolution as measured from $Z \rightarrow e^+e^-$events and compared to simulation (right). Events are categorized according to the electron class and pseudorapidity region of each leg (G1: electron *golden* or *bigbrem*, G2: electron *showering* or *crack* or *badtrack*, EB: electron in ECAL barrel, EE: electron in ECAL endcaps). Results are presented for data collected at $\sqrt{s}$ = 8 TeV.

A.1.2 Muons

Muon reconstruction

Muon tracks are reconstructed independently as a *track* in the inner tracker and as a *standalone-muon track* in the muon system alone. The two objects, if matched in direction and momentum, are re-fit to form a *global muon* object. As very low p_T muons may not have sufficient energy to penetrate the entire muon system and leave track segments in one or two stations of the muon system, tracks matched to such segments form *tracker muon* objects. Both global and tracker muons are used in the presented analysis. More details on muon reconstruction in CMS can be found elsewhere [29].

Momentum scale and resolution

The p_T measurement resolution for muons in the p_T range relevant for the observed Higgs boson candidate with a mass near 125 GeV is mostly defined by the accuracy of muon hit localization in the inner track, which is in turn mostly dominated by the multiple scattering of muons in the tracker material. The instrumental accuracy of the muon hit measurements and the overall alignment contribute too, but at a sub-leading level.

Calibration of residual differences in energy scale and resolution between data and simulation

The momentum determination of muons is affected by small differences in the alignment geometries of the tracker used, both in data and simulation. The misalignment of the tracker results in a charge (Q), pseudorapidity (η), and azimuth angle (ϕ) dependence in the reconstructed muon momentum for both samples.

In general, an overall momentum scale bias (e.g. error in the magnetic field) should be identical for positive and negative muons. Misalignment would results in a difference in the mean $1/p_T$ between positive and negative muon. A first correction factor $C^{Data/MC}(Q,\eta,\phi)$ is defined as the difference in the mean $1/p_T$ between an ideal perfectly aligned simulation and reconstructed data (or reconstructed simulation).

$$C^{Data/MC}(Q,\eta,\phi) =< 1/p_T^{MC(gen)}(Q,\eta,\phi) > - < 1/p_T^{Data/MC(reco)}(Q,\eta,\phi) > \quad (7)$$

A correction D_m factor that accounts for possible mismodeling of the integral of $B \cdot dL$ is defined as the average correction factor $C^{Data/MC}$ between positive and negative muons, and a correction factor D_a which accounts for the misalignment is defined as the difference between negative and positive muon correction factors. The final correction factor is then expressed as a combination of D_m and D_a. After the above correction, an extra global factor is applied on both simulation and data to set the Z mass to equal the MC Z mass after FSR. Also, additional smearing is applied to the simulation to match the measured widths of Z distribution in the data.

The observed disagreement between data and simulation for the transverse momentum distribution of the Z boson at low p_T implies that the POWHEG generator with PYTHIA parton showering should be tuned. A correction is applied to the simulation at the generator level such that the transverse momentum distribution of the Z matches the data. The correction factor is obtained comparing the Z p_T spectrum between the data and simulation after the first iteration. Once the transverse momentum distribution of the Z in POWHEG has been tuned to match the data, the above analysis is repeated and muon momentum corrections are updated.

The corrections mentioned above calibrate the overall momentum scale and remove the dependency of the scale on the $1/p_T$, η, ϕ and charge of the muon, thereby improving also the momentum resolution.

In the central part of the detector and for the lepton momentum range $p_T < 100$ GeV relevant for this analysis the typical muon momentum resolution after the above energy correction and smearing is $\delta p_T / p_T \sim 1-3\%$, as shown in Fig. 17. The quoted numbers represent the Gaussian core of the reconstructed energy-momentum distribution, which also exhibits a tail toward lower end. The tail arises from the unaccounted bremsstrahlung radiation, both internal and induced by the interactions of muons with the detector material.

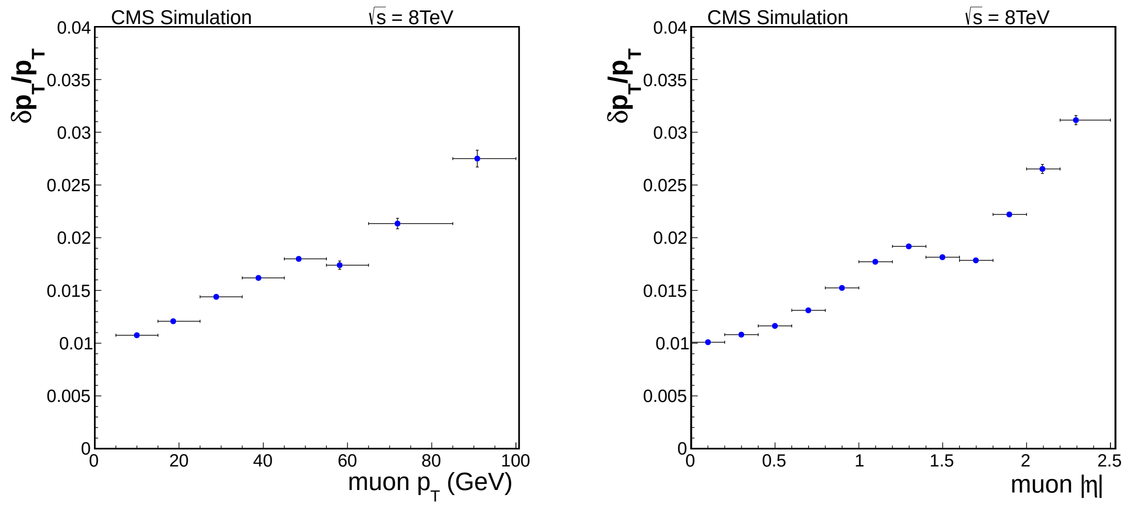

Figure 17: Expected resolution for prompt muons as a function of p_T (left) and $|\eta|$ (right). Events are from a simulated Higgs sample ($m_H = 126$ GeV). The resolution is defined as the sigma of double Crystal Ball function that describes the reconstructed p_T distribution around the true p_T.

Validation

The muon p_T scale and resolution after the calibration are also validated in data using di-muons from J/ψ, Y and Z decays, to cover the full momentum range relevant for the $H \to 4\ell$ search. Muons with $p_T > 5GeV$ are considered. For $Z \to 2\mu$ events, all muon selection criteria as used in the $H \to ZZ \to 4\ell$ analysis are also applied.

The events are separated in categories according to the average p_T and $|\eta|$ of the two muons, and the di-muon mass distributions in each category are fitted with a BW convoluted with a CB function to extract the offset in the measured peak position in data, $\Delta m^{\mathrm{CB}}_{\mathrm{data}}$, with respect to that observed in the simulation, $\Delta m^{\mathrm{CB}}_{\mathrm{MC}}$. Similarly, we compare differences in the instrumental width of the peak as seen in data, $\sigma^{\mathrm{CB}}_{\mathrm{data}}$, to that observed in the simulation, $\sigma^{\mathrm{CB}}_{\mathrm{MC}}$.

Figure 18 shows the results presented in terms of the relative difference between data and simulation:

$$\frac{\Delta m}{m} = \frac{\Delta m^{\mathrm{CB}}_{\mathrm{data}} - \Delta m^{\mathrm{CB}}_{\mathrm{MC}}}{m_Z}, \qquad \frac{\Delta \sigma}{\sigma} = \frac{\sigma^{\mathrm{CB}}_{\mathrm{data}} - \sigma^{\mathrm{CB}}_{\mathrm{MC}}}{\sigma^{\mathrm{CB}}_{\mathrm{MC}}}. \tag{8}$$

After the calibration, the relative momentum scale between data and simulation is consistent within 0.1%. A somewhat larger offset is seen for J/Ψ events with two high p_T muons in the very forward direction. For these events, di-muons are nearly collinear and such kinematic configuration is very atypical for $H \to ZZ \to 4\ell$ events; and hence the observed larger mass scale offset observed for such events is irrelevant in the context of the Higgs analysis. The instrumental Z-peak mass resolution observed in data is consistent with the simulation within about 10% (Fig. 18, right).

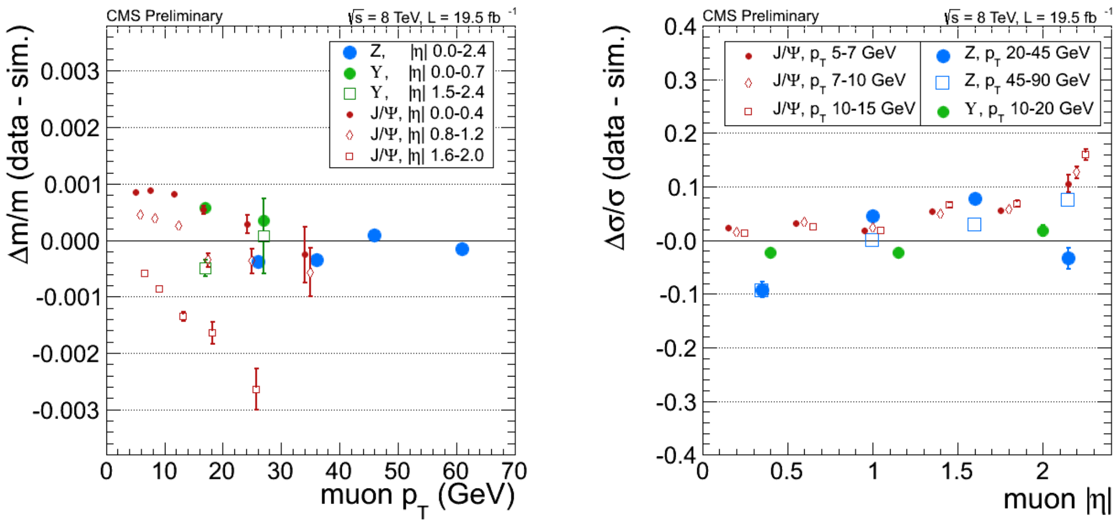

Figure 18: Relative difference between the di-muon mass scales (left) and resolutions(right) in data and simulation extracted from J/Ψ, Υ and Z decays, as function of the average muon p_T (left) and $|\eta|$ (right) for the 2012 data. The uncertainties shown are statistical only.

A.2 Event-by-event multi-lepton mass resolution

As shown in the previous section, the quality of the momentum measurement of individual leptons can substantially vary, depending on their direction, p_T, number of reconstructed hits for muons or amount of bremsstrahlung for electrons. This entails that the four-lepton invariant mass resolution for $\mathrm{H} \to 4\ell$ decays varies broadly as well, by as much as a factor of 2-3. Therefore, mixing indiscriminately events with well and poorly measured four-lepton masses would hinder Higgs boson mass measurements, making them less accurate on average than they can be if individual events in the mass fit are properly weighted according to their estimated mass resolutions $\sigma_{m_{4\ell}}$. Moreover, the determination of the mass resolution for each event entering the fit allows us to assign the proper uncertainty to the measured mass.

Propagation of per-lepton momentum uncertainties to the multi-lepton invariant mass resolution

The four-lepton mass is reconstructed from leptons' four-vectors evaluated from their basic reconstructed parameters p_T, η, ϕ. Individual lepton uncertainties are computed from the weights for the combined momentum and taken from the track fit for the angles in the case of electrons, while the full covariance matrix from the track fit is used for muons. The propagation of individual uncertainties on reconstructed leptons' kinematic parameters (σ_{p_T}, σ_η, σ_ϕ) into an uncertainty on the four-lepton mass, $\sigma_{m_{4\ell}}$, is done including all errors and their correlations. The contribution of uncertainties on lepton's η and ϕ to the four-lepton mass uncertainty are found negligible with respect to the uncertainties on lepton's p_T, as expected.

Calibration of per-lepton momentum uncertainties

As previously described, electron momentum uncertainties are inflated to account for the additional smearing needed to match the observed width at the $\mathrm{Z} \to \mathrm{e}^+\mathrm{e}^-$peak. Muon momentum uncertainties are further corrected examining the pull distributions as a function of p_{T} and pseudorapidity. The corrections range between ~ 0.7 and ~ 1.5 and are smaller for low p_{T} muons.

Additional correction factors are derived to accommodate the extra broadening of the di-lepton mass due to the non-Gaussian tails in the single-lepton p_T measurements due to potential unrecovered final state radiation or bremsstrahlung in the tracker or arising from the presence of non-uniform lepton energy scale biases as a function of the lepton kinematic and quality. The $Z \to 2\ell$ mass line shape is modeled by a Breit-Wigner function convoluted with a Crystal Ball function, with the Breit-Wigner function parameters fixed to the nominal Z mass and natural Z width. For the Crystal Ball function, the σ_{CB} is set to be the product between a correction factor λ and δm, where δm is the event-by-event mass resolution including the correction on the per-lepton momentum uncertainties mentioned in the previous section. The correction factors λ extracted by fitting the above model to the Z line shape are summarized in Table 4 for both 2011 and 2012 data and simulation.

Table 4: Correction factors for the per-lepton momentum uncertainties derived from Z and J/Ψ events in data and simulation. For electrons in 2012 data a slightly different binning in $|\eta|$ is used, $[0.0, 1.0, 1.5, 1.9, 2.5]$, as it yields a more uniform correction factor within each bin.

muons, $p_T < 20$	2011 Data	2011 Sim.	2012 Data	2012 Sim.
$\|\eta\| < 0.8$	1.00	1.06	1.03	1.08
$0.8 < \|\eta\| < 1.6$	0.98	1.07	1.01	1.08
$1.6 < \|\eta\| < 2.4$	0.96	1.07	0.99	1.06
muons, $p_T > 20$	2011 Data	2011 Sim.	2012 Data	2012 Sim.
$\|\eta\| < 0.8$	1.09	1.16	1.03	1.07
$0.8 < \|\eta\| < 1.6$	1.16	1.03	1.07	1.05
$1.6 < \|\eta\| < 2.4$	0.95	0.99	1.09	1.03
electrons	2011 Data	2011 Sim.	2012 Data	2012 Sim.
$\|\eta\| < 0.8$	1.25	1.27	1.30	1.27
$0.8 < \|\eta\| < 1.5$	1.16	1.11	1.24	1.22
$1.5 < \|\eta\| < 2.0$	1.30	1.30	1.22	1.17
$2.0 < \|\eta\| < 2.5$	1.16	1.24	1.14	1.13

Validation using $Z \to \ell\ell$ events and extrapolation to 4ℓ events

As a test, $Z \to \ell\ell$ events are used, classified into ten categories based on the mass resolution as predicted from the propagation of per-lepton uncertainties. In each category , a fit of the Z peak is performed and the di-lepton mass resolution is evaluated. Figure 19 shows the results for $Z \to ee$ and $Z \to \mu\mu$ events for the test performed on simulated events (open symbols) and data (closed symbols). The measured and predicted relative di-lepton mass resolutions are found consistent within $\pm 20\%$. We repeat the closure test for sub-groups of events where the two leptons are required to satisfy some additional requirements (e.g. be in different $|\eta|$-directions, be showering on non-showering for electrons, etc.). The predicted and measured mass resolution consistently agree within $\pm 20\%$ uncertainty, except for a few rare, and hence neglected, exceptions where the difference is somewhat above 20%.

The extrapolation to the four-leptons system is validated using simulation. The predicted resolution is seen well correlated with the resolution as extracted from the four-lepton mass distributions in all the sub-channels, with a difference between the two well covered by the $\pm 20\%$ systematic uncertainty.

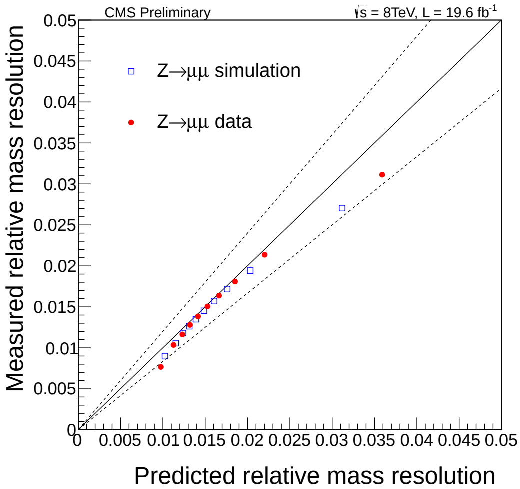

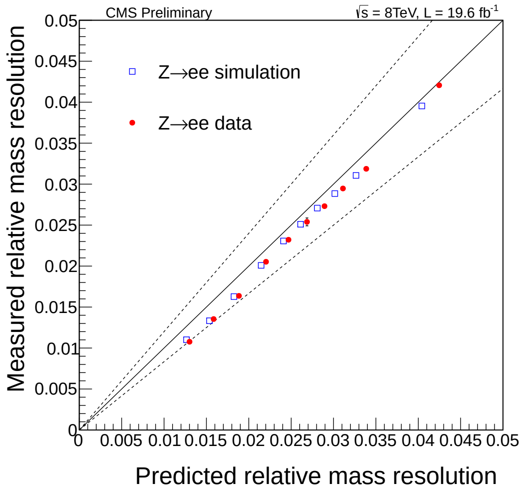

Figure 19: Comparison between the resolution as predicted from the per-lepton uncertainties and the resolution measured from di-lepton mass fit for di-muon (left) and di-electron (right) for data (closed symbols) and simulation (open symbols). The dotted lines indicate a deviation of ±20%. The presented measurement corresponds to the data collected at $\sqrt{s}$ = 8 TeV.

The relative mass uncertainty distribution as measured in the data in a Z→ 4ℓ control region defined as $80 < m_{4\ell} < 100$ GeV is presented in Fig. 20. A good agreement is found and the different contributions from electrons and muons to the resolution in this mass range are visible. The relative mass uncertainty distribution is also checked in a ZZ→ 4ℓ control region and in the Z_1+X control region as defined in Section 5. A good agreement between data and simulation is found, indicating a good control of the mass resolution also for fake leptons. The relative mass resolution distributions are modeled in the statistical analysis using a composition of Landau and log-normal distributions for the 4e final state, and Landau and Gaussian distributions for the 4μ and $2e2\mu$ final states.

A.3 Cross-check using the $Z \to 4\ell$ peak

The $Z \to 4\ell$ decays give a clean resonant peak in low mass part of the four-lepton invariant mass distribution, which can be used as a reference in the context of the measurement of the properties of the new boson. A fit is performed of the four lepton mass distribution in the $Z \to 4\ell$ region. Template signal shapes are obtained from the simulation and fitted using a BW convoluted with a CB. The procedure followed is the same as the one used for the mass measurement of the new resonance (1D model). Figure 21 shows an overlay of the best fit of the four-lepton mass distribution in data. The fitted values for the mass and width of the Z are found compatible with the PDG values within the uncertainties.

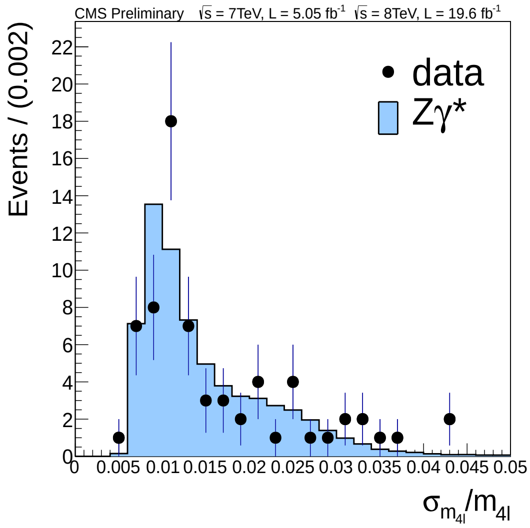

Figure 20: Relative mass error distribution in the data and compared to simulation for events in a $Z \to 4l$ control region ($80 < m_{4\ell} < 100$ GeV). The three final states, 4e, 4μ, and $2e2\mu$, are added together. Results correspond to the data collected at $\sqrt{s}$ = 7 TeV and $\sqrt{s}$ = 8 TeV.

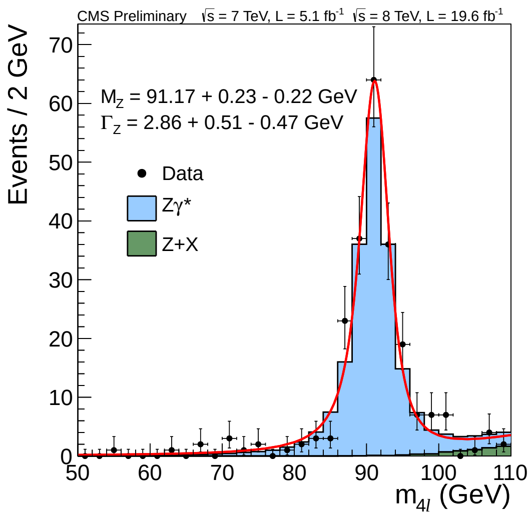

Figure 21: Four-lepton mass distribution in the mass range $50 < m_{4l} < 110$ GeV. Data are shown with points. The three final states, 4e, 4μ, and $2e2\mu$, are added together. The solid line represents an overlay of the best fit obtained using the same technique as for the mass measurement of the new boson. Expectation from simulation is shown by the colored histograms. Results correspond to the data collected at $\sqrt{s}$ = 7 TeV and $\sqrt{s}$ = 8 TeV.